ORNL/TM-2015/584

Embedded Sensors and Controls to Improve Component Performance and Reliability – Bench-scale Testbed Design Report

Alexander M. Melin
Anis Drira
Roger Kisner
F. Kyle Reed
David L. Fugate

September 2015

OAK RIDGE NATIONAL LABORATORY
MANAGED BY UT-BATTELLE FOR THE US DEPARTMENT OF ENERGY

ORNL/TM-2015/584

Electrical and Electronics Systems Research Division

EMBEDDED SENSORS AND CONTROLS TO IMPROVE COMPONENT PERFORMANCE AND RELIABILITY – BENCH-SCALE TESTBED DESIGN REPORT

Alexander Melin
Anis Drira
Roger Kisner
F. Kyle Reed
David Fugate

Date Published: September 2015

Prepared by
OAK RIDGE NATIONAL LABORATORY
P.O. Box 2008
Oak Ridge, Tennessee 37831-6285
managed by
UT-Battelle, LLC
for the
US DEPARTMENT OF ENERGY
under contract DE-AC05-00OR22725

CONTENTS

LIST OF FIGURES

LIST OF TABLES

ACRONYMS

AMB	Active Magnetic Bearing
ASI	Advanced Sensors and Instrumentation
DOE	Department of Energy
I&C	Instrumentation and Control
ICS	Industrial Control Systems
LQG	Linear Quadratic Gaussian
LQI	Linear Quadratic Integrator
LQR	Linear Quadratic Regulator
NASA	National Aeronautics and Space Administration
NEET	Nuclear Energy Enabling Technologies
ORNL	Oak Ridge National Laboratory
PID	Proportional Integral Derivative

ABSTRACT

Embedded instrumentation and control systems that can operate in extreme environments are challenging to design and operate. Extreme environments limit the options for sensors and actuators and degrade their performance. Because sensors and actuators are necessary for feedback control these limitations mean that designing embedded instrumentation and control systems for the challenging environments of nuclear reactors requires advanced technical solutions that are not available commercially. This report details the development of testbed that will be used for cross-cutting embedded instrumentation and control research for nuclear power applications. This research if funded by the Department of Energy's Nuclear Energy Enabling Technology program's Advanced Sensors and Instrumentation topic. The design goal of the bench-scale testbed is to build a re-configurable system that can rapidly deploy and test advanced control algorithms using a hardware in the loop framework. The bench-scale testbed uses active magnetic bearings as the electro-mechanical system which require the use of feedback control to function. Active magnetic bearings are a technology that can reduce failures and maintenance costs in nuclear power plants. They are particularly relevant to liquid salt reactors that operate at high temperatures (700 °C). Pumps used in the extreme environment of liquid salt reactors provide many engineering challenges that can be overcome with magnetic bearings and their associated embedded instrumentation and control. This report will give details of the mechanical design, electromagnetic design, geometry optimization, power electronics, and initial control system design.

1 INTRODUCTION

Many technologies used in power generation and other industries are often required to work in extreme environments such as high temperatures, high magnetic fields, or corrosive liquids. The restrictions on materials and physical properties mean that many of the systems used are passive mechanical systems with limited available sensing. Increasingly however, the large performance and reliability improvements that come from active control have been recognized. This requires sensors, actuators, and electronics that can operate in extreme environments which many times are not available commercially. Often times too, the performance of sensors in extreme environments is degraded through mechanisms such as drift and noise that make utilizing them for feedback control difficult. This document provides details about the design of a bench-scale active magnetic bearing testbed that is intended to investigate embedded instrumentation and controls (I&C) for extreme environments. This research is sponsored by the Department of Energy's (DOE) Nuclear Energy Enabling Technology (NEET) cross-cutting technology development program under the Advanced Sensors and Instrumentation (ASI) topic. Specific objectives for the embedded I&C project are as follows.

- Explore and quantify the potential gains from embedded I&C – improved component reliability, increased performance, and reduced cost.
- Identify practical control, sensing, and measurement techniques for the extreme environments found in high-temperature reactors.
- Design and fabricate a functional prototype high-temperature pump for liquid fluoride salts – represents target demonstration of improved performance and reliability and has great potential for widespread usage beyond salt reactor applications.

The design goal of the bench-scale testbed is to build a re-configurable system that can rapidly deploy and test advanced control algorithms in a hardware in the loop setup. The bench-scale testbed will be designed as a fluid pump analog that uses active magnetic bearings to support the shaft. The testbed represents an application that would improve the efficiency and performance of high temperature pumps for liquid salt reactors that operate in an extreme environment and provide many engineering challenges that can be overcome with embedded instrumentation and control.

High temperature liquid salt reactors provide benefits over other traditional reactors designs. They operate at much lower pressures and have passive safety features based on the physics of the reactor design. However, the liquid salt reactors will operate at 650 °C and the liquid salt coolant is corrosive to some metals. This environment greatly limits the options for sensing and actuation because the operating temperature is above the Curie temperature for most materials and many commercial sensors utilize materials that are chemically incompatible with the liquid salt. Fortunately, some materials exist that still maintain the needed physical, chemical, or electromagnetic properties in the extreme environment of a liquid salt reactor and can be used as sensors and actuators so that a feedback control system can be implemented. A coolant pump was chosen as the embedded I&C testbed because pumps represent one of the main maintenance costs in nuclear power plants and one of the main points of failure. Improving their reliability and increasing their performance through the use of embedded I&C will have a large impact on the safety and cost of operating a nuclear power plant. The environmental effects of the liquid salt lead to some atypical design features for the pump. First, pump bearings and seals are the largest point of failure and their lifetime will be further decreased in a high temperature liquid salt environment. This leads to the design choice to use active magnetic bearings (AMBs) in the pump. Second, the materials that maintain their electromagnetic properties needed for AMBs that will function at the reactor operating temperatures are chemically incompatible with the liquid salt, so the rotor and stator need to have protective 'cans' surrounding them to prevent any corrosion of the rotor and stator materials. This type of pump is known colloquially as a canned rotor pump.

Previous work developing high temperature AMBs has taken place mainly in the aerospace field such as the National Aeronautics and Space Administration (NASA) work in 2006 on a radial magnetic bearing that could operate at 540 °C [5]. More recently, there has been active European research into the mechanical design of magnetic bearings that can operate at temperatures of up to 550 °C [2]. In [3], the authors developed the conceptual design of a 700 °C AMB canned rotor pump. In [4] the authors develop the control theory for controlling an AMB with fluid in the airgap between the rotor and stator that causes large coupling forces between the radial bearing axes.

The goal of this project is not specifically the design of high temperature active magnetic bearings, but an investigation of the quantifiable benefits that arise from utilizing embedded I&C in extreme environments. Ancillary benefits of this research are a higher achievable operating temperature for active magnetic bearings than currently exists, sensorless control of AMBs where the rotor is submerged in fluid causing nonlinear coupling between the rotor axes, and control of an AMB where there is a protective can around the rotor that causes a low pass filter effect due to eddy current losses. The testbed will be used to compare stability margins, performance, and limitations of different control algorithm design techniques such as de-coupled proportional integral and derivative (PID) controllers, linear quadratic Gaussian controllers (LQG), or Robust controllers.

This document is organized as follows. Chapter 2 will outline the mechanical design of the bench-scale testbed. Chapter 3 will give details concerning the testbed electromagnetic design. Chapter 4 will provide information on the control system hardware, software, and algorithms. Finally, Chapter 5 will discuss

conclusions and future work.

2 MECHANICAL DESIGN

The goal of the testbed design was to provide a flexible platform for hardware in the loop testing of embedded I&C. The testbed requirements for flexible operation and safety lead to the following design features:

- Easily changeable rotor and stator laminations,
- Touch-down bearings to protect the rotor and stator,
- External position sensors,
- Variable axial spacing between bearings,
- External shaft torque,
- Optical table mount.

The easily changeable rotor and stator laminations allow different lamination materials to be tested with and without protective cans, with varying airgaps between the stator and rotor, and multiple stack lengths. The external position sensor are high precision and high bandwidth sensors that will be used for the initial feedback control stabilization of the rotor and to test and validate sensorless bearing control techniques. The variable axial spacing between bearings will allow different physical configurations and different shaft moments of inertia and mode shapes to be tested to study the sensitivity of the controller to variations in these parameters. External shaft torque is supplied by a flexible coupling to an induction motor for testing the effect of rotational velocity and shaft imbalance on the stability and performance of different feedback control designs. To provide stability and options for precision measurement, the testbed is designed to be mounted to an optics table. Figure 1 shows a rendering of the final testbed design and Figure 2 shows a cross sectional view of the final testbed design.

The bench-scale testbed design consists of a baseplate that bolts to an optical table for rigidity. The other components of the testbed are designed to be modular and clamp to the baseplate. The touchdown bearings are mounted to towers and held in place by bearing tolerance rings that provide some damping when the shaft contacts the touchdown bearing. The external position sensors are mounted to the tower that houses the touchdown bearings so that they are spaced at opposite ends of the shaft and there is no physical contact with the shaft when it is levitating. Two radial AMBs are used to control the radial movement and tilt of the shaft. The two radial AMBs are located on either side of an axial AMB that controls the shaft's axial movement. Everything is mounted by high precision shoulder bolts and shaft collars that allow different stator and rotor configurations to be used. The radial magnetic bearings utilize split stators to minimize stray magnetic fields that can cause coupling between the axes. Figure 3 shows an exploded view of a radial bearing.

The testbed design utilizes some parts that were made using additive manufacturing. Specifically, the sensor mounts and the covers and tie-downs for the stator coil wires were printed in ABS using a 3-D printer. The testbed assembled without sensors is shown in Figure 4.

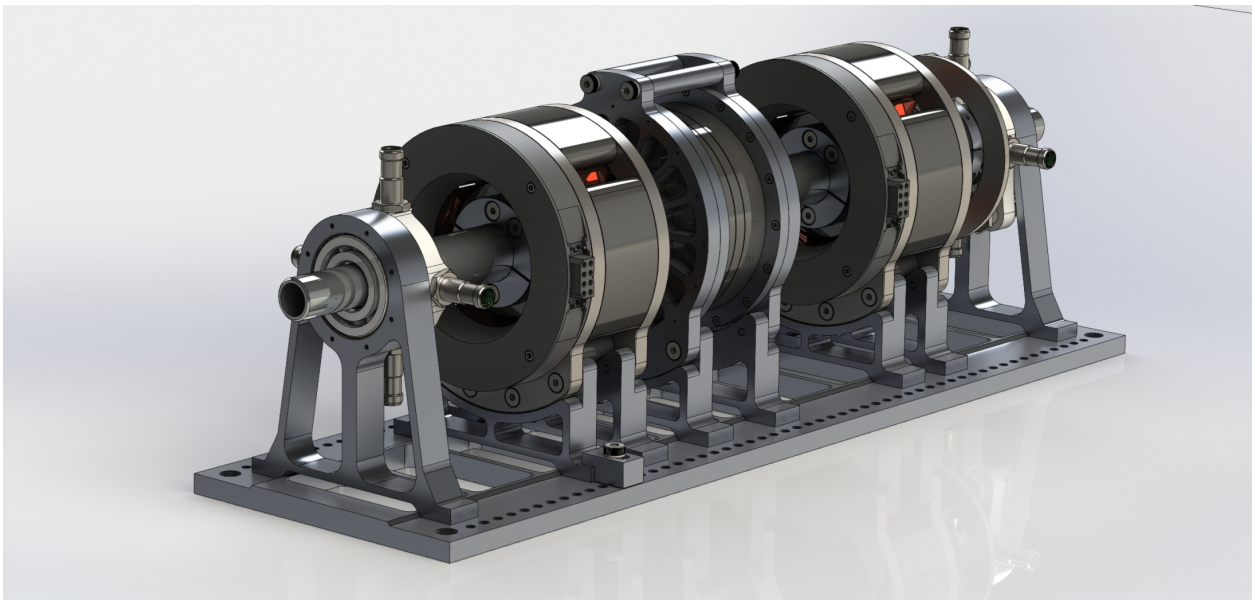

Fig. 1. Final bench-scale testbed design.

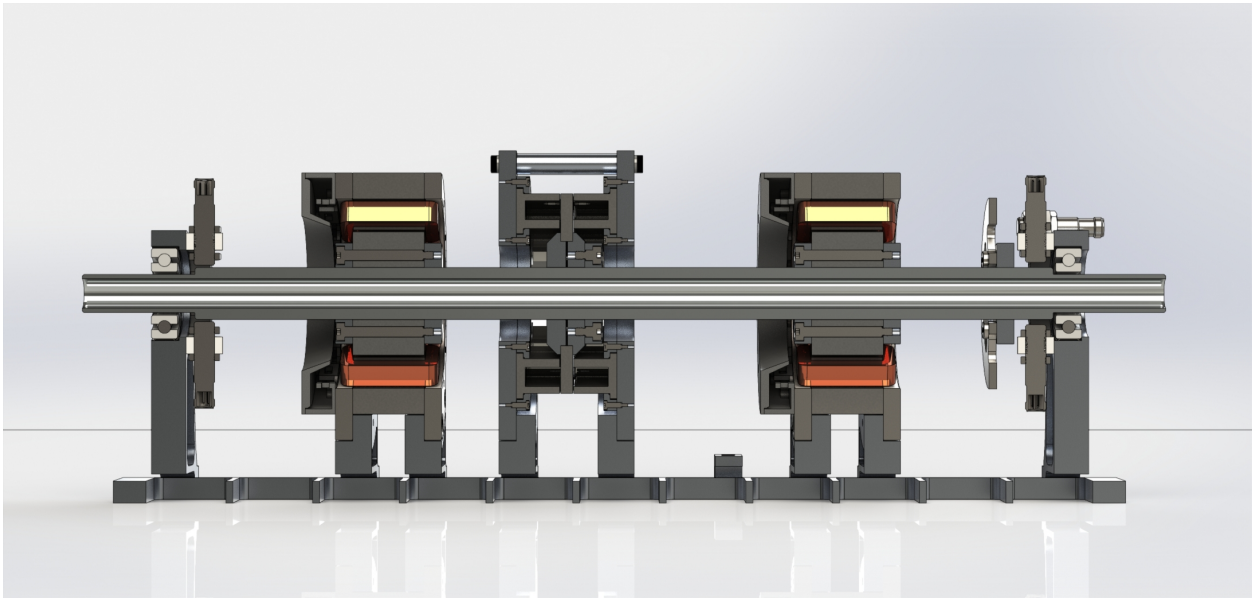

Fig. 2. Cross-section view of the final bench-scale testbed design.

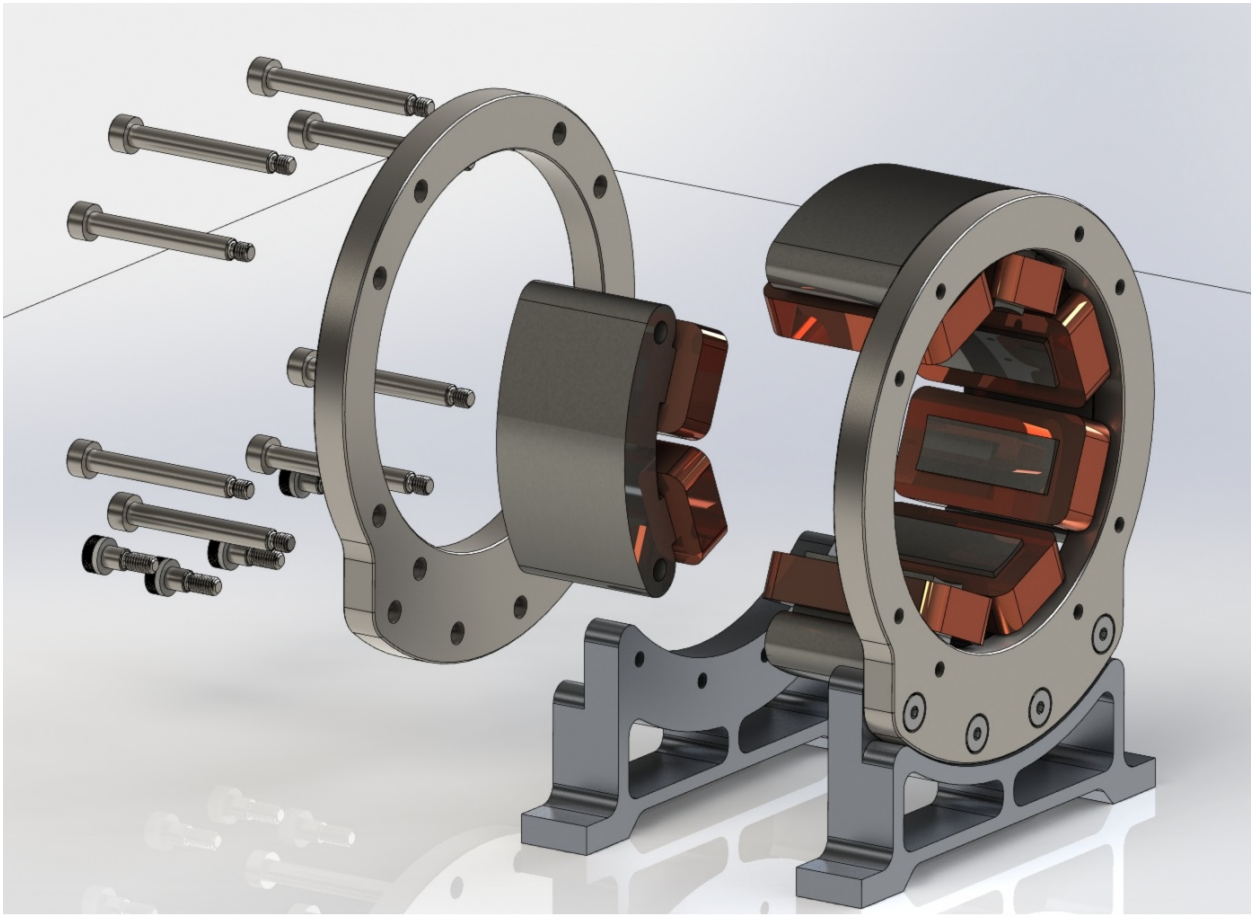

Fig. 3. Exploded view of a radial bearing stator.

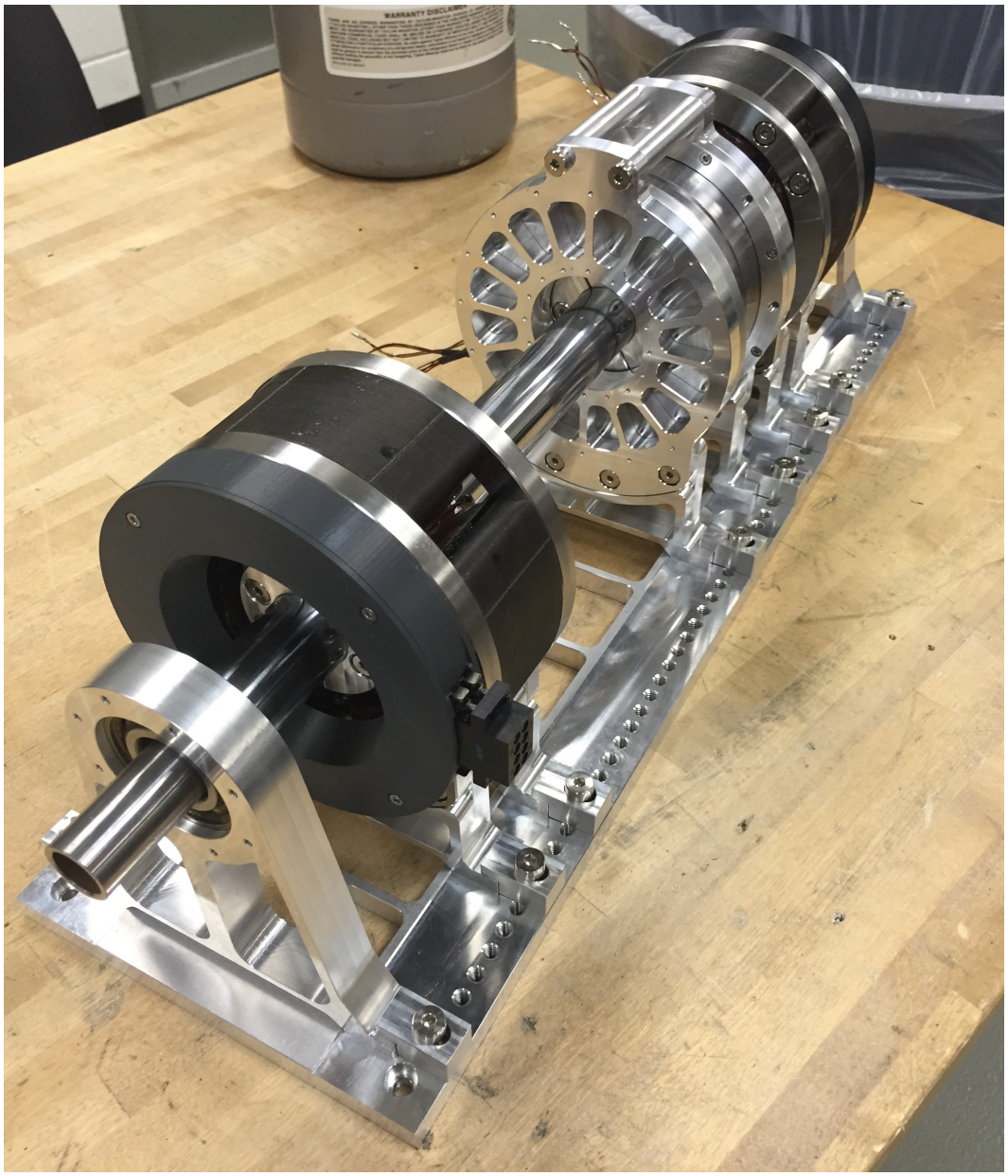

Fig. 4. Assembled testbed without sensors or power electronics.

3 ELECROMAGNETIC DESIGN

In parallel with parametric mechanical design of the testbed accomplished as detailed in Chapter 2, the optimization of the electromagnetics and bearing geometry was undertaken. The main goal of the electromagnetic design was to meet the force requirements of the system while minimizing the overall weight of the testbed for portability. The force requirements are bounded by the shaft weight and the magnitude of potential disturbance forces on the shaft. For the testbed, the shaft weight and imbalances when rotating are the two major forces and are the main driver for the force characteristics. The main requirement is that the radial bearings are able to generate enough force to counteract the shaft weight when the shaft is resting on the touchdown bearings. This is the largest airgap between the stator and rotor and when the shaft is centered, this configuration will have a larger maximum achievable force that will be used for disturbance rejection.

3.1 AMB Design Optimization

This section presents the design calculations used to optimize the bench-scale testbed active magnetic bearing geometry. The simple electromagnetic circuit for the AMB make the direct calculation of the magnetic forces and parametric optimization over the AMB geometry parameters feasible. The general design goal for the bench-scale testbed is to minimize the shaft weight and overall weight of the testbed while maximizing the AMB force achievable and remaining within the geometric constraints of the design.

3.1.1 Parametric AMB Geometry

To perform a parametric optimization of the AMB magnetic circuit, the stator and rotor geometry are defined using the following parameters.

- s_0 - air gap between the stator and rotor
- w_t - width of a stator tooth
- w_y - width of the stator yoke
- h_t - height of a stator tooth
- l_s - axial length of the stator and rotor stacks
- d_r - diameter of the rotor
- d_s - diameter of the shaft
- θ_t - angle between two teeth in the stator

The geometry parameters listed are used to calculate the total flux path lengths through the stator and rotor. The flux path for the stator is given by the equation

$$l_s = 2h_t + w_y + \theta_t \left(\frac{d_r + w_y + s(s_0 + h_t)}{2} \right) \tag{1}$$

The flux path length through the rotor is given by the equations

$$\gamma_a = \theta_t - 1 - \frac{d_s}{d_r} \tag{2}$$

$$\gamma_b = \frac{1}{2}\left(1 - \frac{d_s}{d_r}\right) \tag{3}$$

$$f_H = \frac{d_r}{2}(1 - \cos(\gamma_b)) \tag{4}$$

$$l_r = \frac{\gamma_a}{4}(d_r - d_s) + \frac{\pi}{4}(d_r - d_s) - 2f_H \tag{5}$$

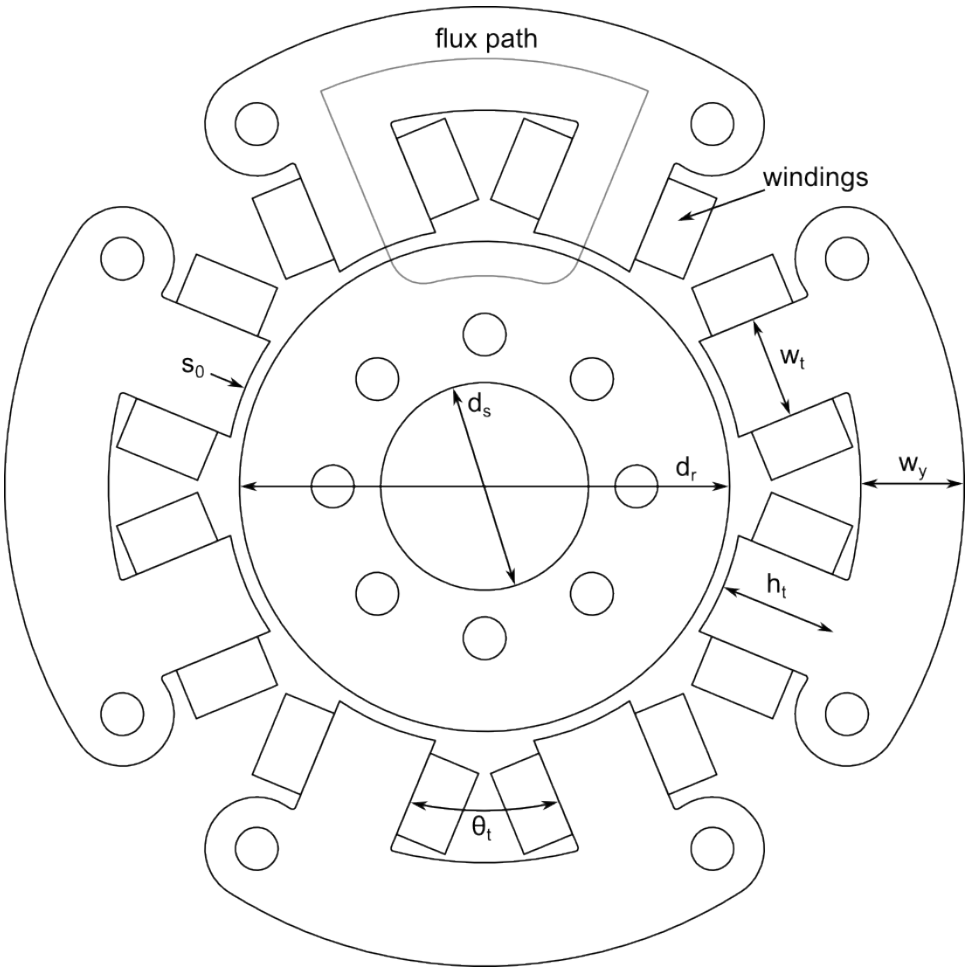

Fig. 5. Dimensions used in the calculation of the flux path lengths.

If the stator has n teeth in total, the angle between two teeth is given by

$$\theta_t = 2\pi/n \tag{6}$$

To calculate the weight of the rotor and stator, we need to calculate their cross sectional areas. The cross sectional area of the rotor is given by

$$A_r = \frac{\pi}{4}(d_r^2 - d_s^2) \tag{7}$$

The area of a single tooth A_{tooth} can be calculated using the following equations

$$\theta_1 = 2sin^{-1}\left(\frac{w_t}{d_r + 2s_0}\right) \tag{8}$$

$$\theta_2 = 2sin^{-1}\left(\frac{w_t}{d_r + 2s_0 - 2w_y}\right) \tag{9}$$

$$A_1 = \frac{(d_r + 2s_0)^2(\theta_1 - \sin(\theta_1))}{8} \tag{10}$$

$$A_2 = \frac{(d_r + 2s_0 + 2w_t)^2(\theta_2 - \sin(\theta_2))}{8} \tag{11}$$

$$h_1 = \frac{d_r + 2s_0}{2} - \sqrt{\left(\frac{d_r + 2s_0}{2}\right)^2 - \frac{w_t^2}{4}} \tag{12}$$

$$h_2 = \frac{d_r + 2s_0 + 2w_t}{2} - \sqrt{\left(\frac{d_r + 2s_0 + 2w_t}{2}\right)^2 - \frac{w_t^2}{4}} \tag{13}$$

$$l_t = h_t + h_1 - h_2 \tag{14}$$

$$A_{tooth} = w_t l_t - A_1 + A_2 \tag{15}$$

Finally, the stator cross sectional area is given by

$$A_{stator} = \frac{\pi}{4}[(d_r + 2(s_0 + h_t + w_y))^2 - (d_r + 2(s_0 + h_t))^2] + nA_{tooth} \tag{16}$$

where n is the number of teeth in the stator. This leads to the mass of the stator given by

$$m_s = \rho A_{stator} l_s \tag{17}$$

We will use two methods to calculate the area available for winding. The first method assumes that the maximum area in the pocket between the teeth is available for winding giving the windings a trapezoidal cross-sectional area. The second method assumes that the windings are pre-wound on a bobbin and slipped over the tooth giving them a rectangular cross-sectional area. The second method is obviously the more conservative method. The maximum winding area is given by

$$W_{max} = \frac{\theta_t}{8}[(d_r + 2s_0 + 2h_t)^2 - (dr + 2s_0)^2] \tag{18}$$

The more realistic winding area using bobbins is given by

$$W_{bobbin} = \frac{h_t}{2}\left[(d_r + 2s_0)\sin\left(\frac{\theta_t}{2}\right) - w_t\right] \tag{19}$$

The number of turns that can fit into the space between the teeth is given by

$$N = f_p \frac{W_{bobbin}}{d_w} \tag{20}$$

where d_w is the diameter of the wire and f_p is the packing fraction. The packing fraction can vary considerably depending on the winding method used. Typical values range from 0.3 to 0.7. The force created by a single radial magnetic bearing is given by the equation

$$F = \mu_0 N^2 A \frac{i^2}{s^2} \cos(\theta_t/2) \tag{21}$$

The optimization objective is

$$\max_{w_t, w_y, h_t \in C} \frac{F}{m} = \frac{\mu_0 N^2 A i^2 \cos(\theta_t/2)}{\rho l_s A_{stator} s^2} \tag{22}$$

Generally speaking there are two optimization problems, optimizing the stator cross sectional geometry (i.e. flux path width and number of turns) and optimizing the length of the rotor and stator stack. Optimizing the the stator cross sectional geometry requires balancing the width of the teeth with the number of turns that can fit in the area between the teeth. As the width of the teeth is increased, the cross sectional area A is increased and the corresponding force is also increased at the cost of increased mass and decreased area for windings. Similarly, as the length of the teeth are increased, the area for windings increases along with the mass of the stator. This optimization is also highly dependent on the inner diameter of the stator as this defines the practical width of the winding area which is installed. Optimizing the stack length of the laminations is much more simple. The stator mass is linearly related to the stack length as well as the force so increasing the stack length linearly increases force and the optimization cost function F/m is a constant for a particular cross sectional geometry.

3.1.2 Material Properties

The testbed stator and rotor laminations are made from 29 gauge M19 C5 steel. Figure 6 shows the B-H curve for the M19 steel. The equations that relate the magnetic flux B with the magnetization force H are

$$\mu = \mu_0 + \frac{1}{\exp^{k_1 B^2} + k_2} \tag{23}$$

$$H = \frac{B}{100\mu} \tag{24}$$

where μ_0 is the permeability of air,$k_1 = 2.477$, and $k_2 = 83.03$.

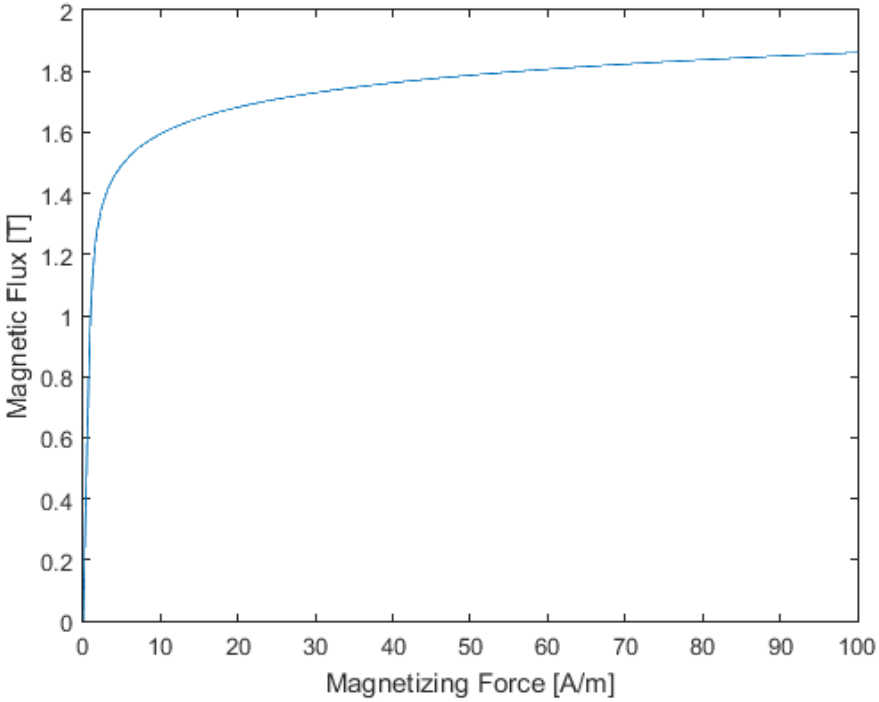

Fig. 6. B-H curve for the M19 steel used in the testbed laminations.

3.1.3 Testbed Force Characteristics

When optimizing the AMB geometry it was assumed that the wire packing factor would be 0.7. This yields the force characteristics given in Figure 7.

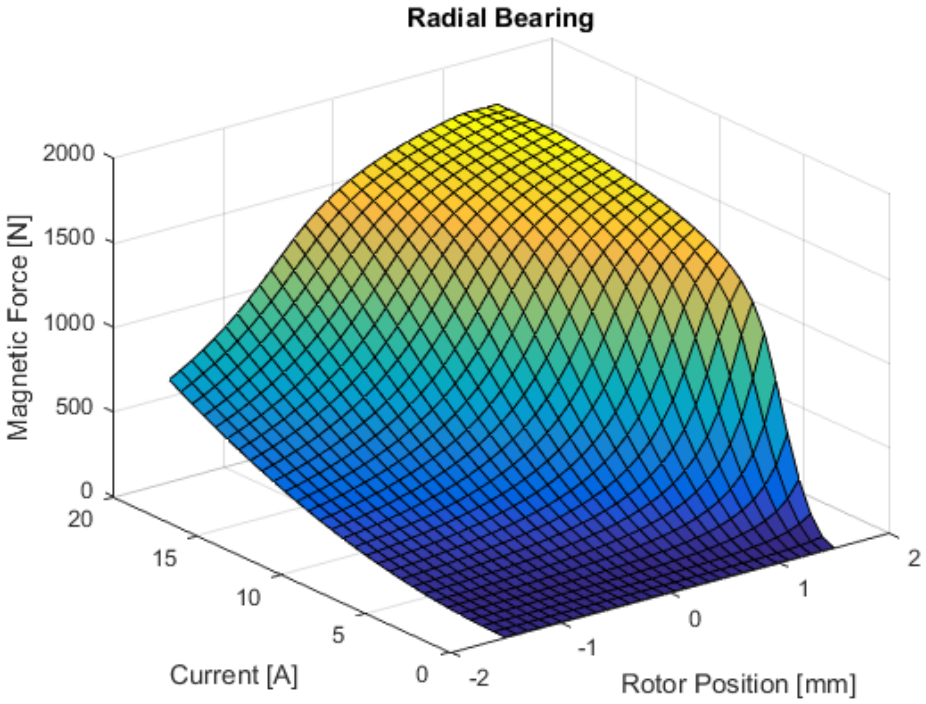

Fig. 7. Radial bearing surfaces as a function of current and airgap

In reality, the windings had a packing factor of 0.32 which gives the calculated force response for the bearing shown in Figure 8. With a shaft weight of approximately $50N$, this puts the force characteristics of the bearing close to the operational limit when the shaft has the maximum airgap because of the $20A$ current limitations on the radial bearings.

3.2 Bench-scale Testbed Physical Parameter

The design geometry chosen after the optimization is given in Table 1. The optimal geometry was chosen using the minimum airgap of $0.0005m$ because the magnetic flux at this rotor position is maximized and can easily become saturated with sub-optimal geometry leading to decreased dynamic response of the bearing.

Figure 9 shows the AMB geometry cost as a function of the tooth height. The optimal tooth height is 15.1 mm.

Similarly, the bearing force as a function of the width of the tooth for three different airgaps is shown in Figure 10.

The axial position of the bearings and sensors can be changed in the testbed so that different physical configurations can be used. The initial testbed physical configuration is shown in Figure 11. This shows the

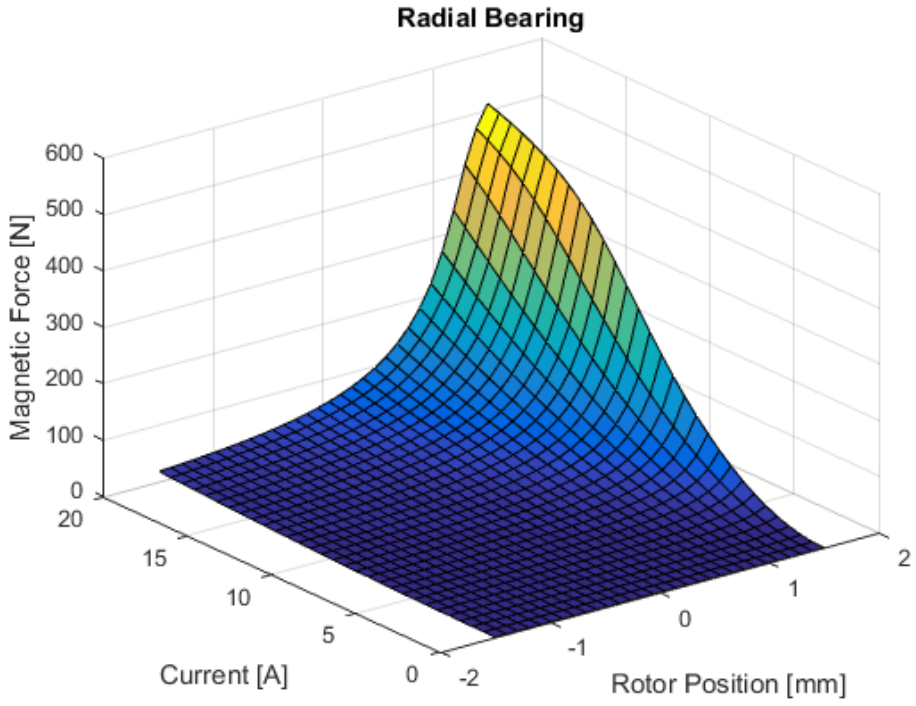

Fig. 8. Radial bearing surfaces as a function of current and airgap

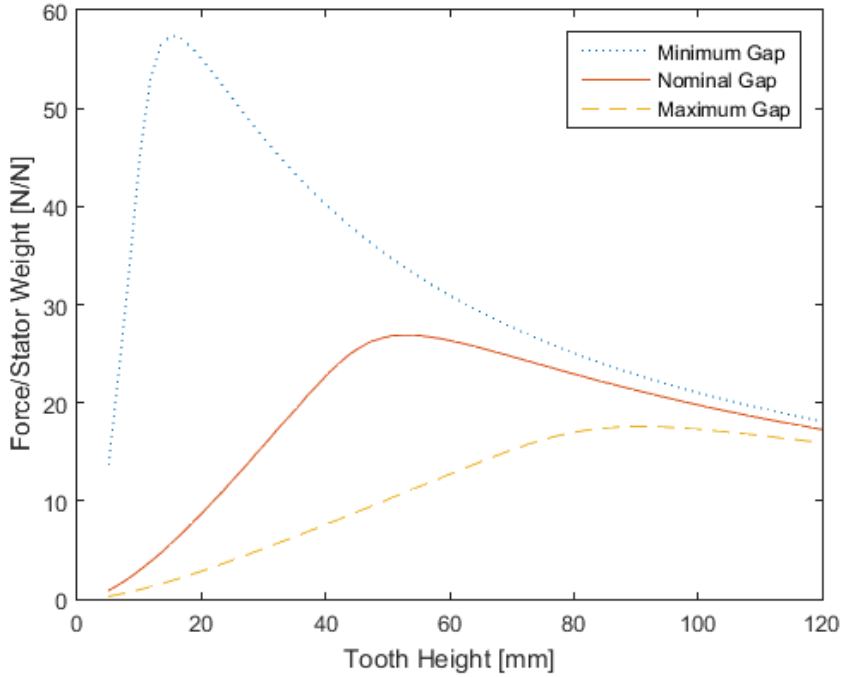

Fig. 9. Bearing size optimization cost as a function of the tooth height h_t.

Table 1. Radial AMB Optimized Geometry

Parameter	Value	Units
s_0	0.002	m
w_t	0.015	m
w_y	0.015	m
h_t	0.017	m
l_s	0.04125	m
d_r	0.071	m
d_s	0.030	m
θ_t	$\pi/4$	rad
L_A	0.14126	m
L_B	0.12348	m
S_A	0.24744	m
S_B	0.23211	m

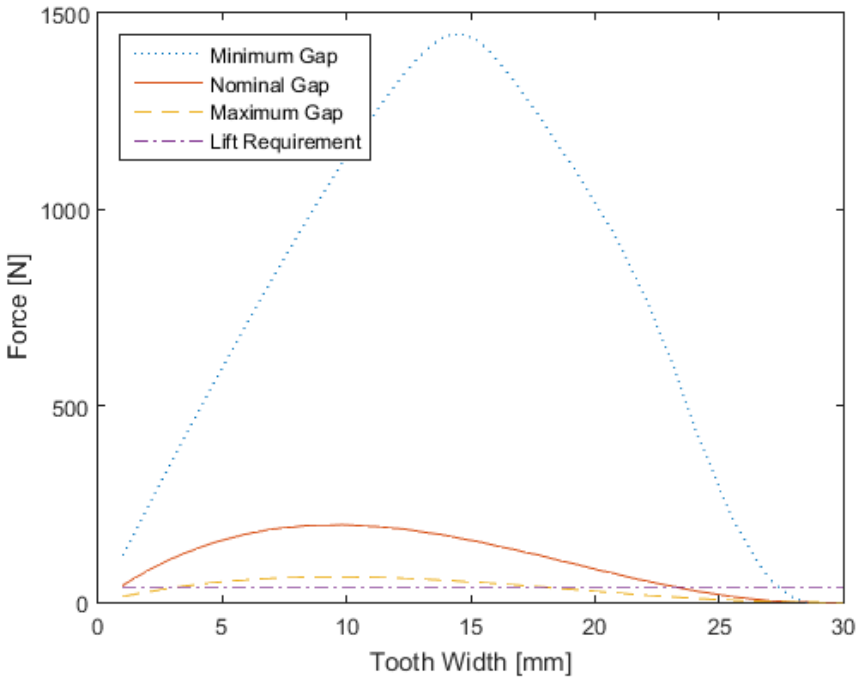

Fig. 10. Bearing size optimization cost as a function of the tooth height h_t.

location of the shaft center of mass and the location of the radial bearings in relationship to the center of mass which define that moments that the bearings exert on the shaft.

Figure 12 shows the locations of the sensors relative to the shaft center of mass. These parameters are used to translate the shaft position measurements into the airgap at the bearing locations.

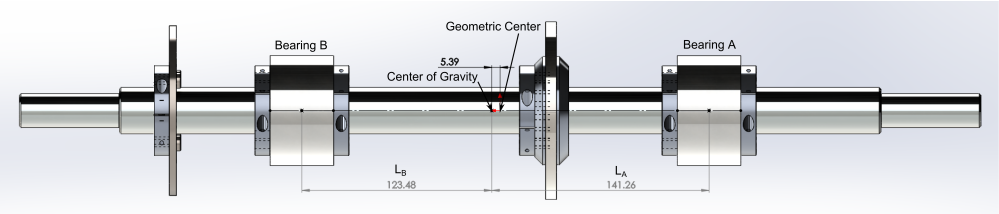

Fig. 11. Location of the center of mass and the radial bearing positions in relation to the center of mass.

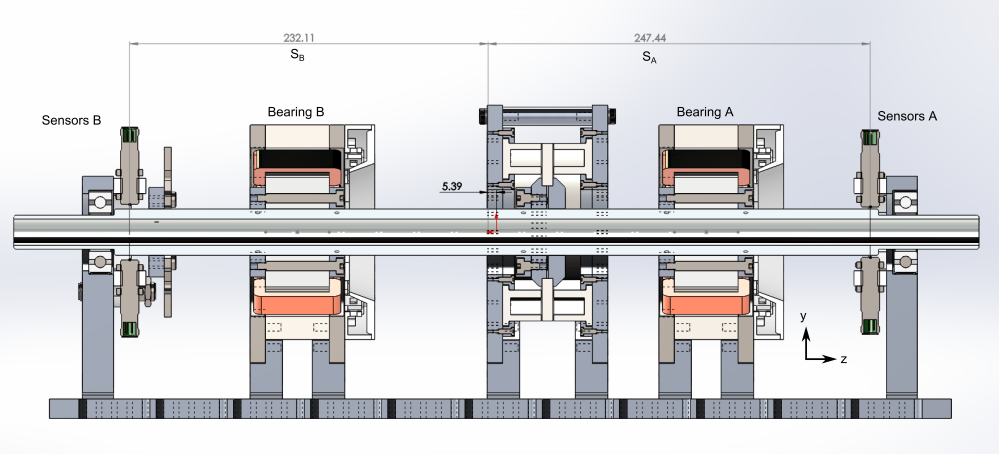

Fig. 12. Sensor locations relative to the shaft center of mass

4 CONTROL SYSTEM DESIGN

4.1 Sensors

For measuring the shaft position, inductive sensors were chosen over capacitive, lasers metrology, and other non-contact sensor techniques. Inductive sensors offered sufficient resolution, accuracy, repeatability, noise rejection, and insensitivity to the target material in a convenient form factor and reasonable price. The specific sensors selected for the testbed are the Baumer IR12.D06S-11123877 shown in Figures 14 and 13. Table 2 gives characteristics of the sensors.

Table 2. Sensor Technical Specification

General Data	
Mounting type	quasi-flush
Measuring distance Sd	$0 \cdots 6\ mm$
Resolution	$< 0,005mm$ (stat.)
	$< 0,01mm$ (dynam.)
Repeat accuracy	$< 0,01mm$
Linearity error	$\pm 720\mu m$ (S=$0 \cdots 6\ mm$)
	$\pm 300\mu m$ (S=$1.5 \cdots 4.5\ mm$)
Temperature drift	± 6 (Full Scale; $-25 \cdots +75°C$)
	± 4 (Full Scale; $0 \cdots +60°C$)
Electrical Data	
Response time	$< 1\ ms$
Voltage supply range $+Vs$	$12 \cdots 36\ VDC$
Current consumption max. (no load)	$10mA$
Output circuit	voltage output
Output signal	$0 \cdots 10\ VDC$
Load resistance	$> 4000\ Ohm$
Short circuit protection	yes
Reverse polarity protection	yes
Mechanical Data	
Type	cylindrical threaded
Housing material	brass nickel plated
Dimension	$12mm$
Housing length	$50mm$
Connection types	connector $M12$
Ambient Conditions	
Operating temperature	$-25 \cdots +75°C$
Protection class	IP67

Fig. 13. Baumer: inductive sensor IR12.D06S-11123877

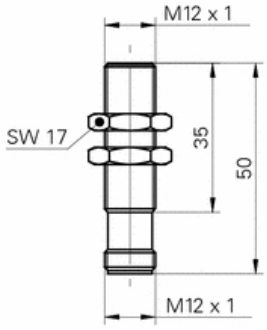

Fig. 14. Baumer: inductive sensor dimension drawing

4.2 Actuators

AMBs use coil windings to develop magnetic flux in the stator magnetic laminations, rotor laminations, and the gap between them forming a magnetic circuit. The flux density B in the magnetic circuit is given by

$$B = \mu_0 \frac{Ni}{2s}, \tag{25}$$

where $\mu_0 = 4\pi \times 10^{-7}$ V-s/A-m is the magnetic permeability of vacuum, N is the number of coil windings, i is the coil current, and $2s$ is the total air gap. This calculation of flux density assumes a constant cross-sectional area of the stator, no flux leakage or other losses, and that the magnetic reluctance in the gap between the rotor and stator is much higher than the reluctance of the laminations.

Assuming each of the eight electromagnets on both radial AMBs have coil currents that can be controlled independently, Eg. (25) for a single coil becomes

$$B_j^k = \mu_0 \frac{Ni_j^k}{s_j^k}, \quad j \in \{x^+, x^-, y^+, y^-\}, \quad k \in \{A, B\}, \tag{26}$$

where s_j^k are the airgaps at each coil.

The force generated by the each magnetic bearing axis is given by

$$F_b = \frac{B^2 A}{\mu_0}, \tag{27}$$

where B is the magnetic flux given by Eq. 26 and A is the cross-sectional area of a magnetic bearing stator tooth. Combining Eq. 26 and Eq. 27 yields

$$F_j^k = \frac{1}{4}\mu_0 N^2 A \frac{(i_j^k)^2}{(s_j^k)^2} \cos\Theta_0 = k\frac{(i_j^k)^2}{(s_j^k)^2} \cos\Theta_0, \quad j \in \{x^+, x^-, y^+, y^-\}, \quad k \in \{A, B\}. \tag{28}$$

4.2.1 Linearization

It is common practice to linearize the magnetic bearing force Eg. (28) to aid in the analytical analysis of the bearing behavior and control system design. This is a valid assumption because of the small movement of the shaft; however, care must be taken to validate any controller developed using the linearized model on the nonlinear model to ensure that the unmodeled dynamics do not destabilize the control system.

By linearizing with respect to both bearing state variables, the linearized force equation for each separate coil can be written as[8]

$$f(x, i) = k_i i - k_s x. \tag{29}$$

The two constants k_i and k_s are calculated by linearizing Eg. (28) around the operating points i_0 and s_0. Assuming that the bearing has rotational symmetry, the constant k_i related to the current is given by

$$k_i = \left.\frac{\partial f}{\partial i}\right|_{i=i_0, s=s_0} = \left. 2k\frac{i}{s^2}\cos\Theta_0 \right|_{i=i_0, s=s_0}. \tag{30}$$

Table 3. Magnetic parameters for the model

Parameter	Value	Units
μ_0	$4\pi \times 10^{-7}$	V-s/A-m
n	32	turns
A_a	6.1875×10^4	
$k = \mu_0 n^2 A_a$	7.9621×10^{-07}	
s_0	0.002	m
i_0	1	A
k_i	4.2665	N/A
k_s	-2133	N/m

Likewise, the spring constant k_s related to the rotor movement is given by

$$k_s = \frac{\partial f}{\partial s}\bigg|_{i=i_0, s=s_0} = -2k\frac{i^2}{s^3}\cos\Theta_0\bigg|_{i=i_0, s=s_0}. \tag{31}$$

Table 3 summarizes the magnetic properties of the system design.

Solving for the i_0 we have the following equation and Table 4 summarizes calculated versus measured values:

$$i_0 = \sqrt{\frac{mgs_0^2}{2k\cos\Theta_0}} \tag{32}$$

Table 4. Calculated versus Measured parameters

s_0	i_0 Calculated	i_0 Measured
0.001	5.8 A	5.4 A
0.0015	8.7 A	7.6 A
0.002	11.6 A	10.8 A
0.0035	20.3 A	18 A

4.2.2 Power electronics

The power electronics for AMB consists of four power supplies, two RSP 2000-24 used for the X-axis and Y-axis, one RSP 750-24 used for Z-axis, and one RS 15-24 used for the sensors. The specification for these power supplies is tabulated in the following Tables (5, 6, 7). The RSP's power supplies are connected to Pololu High-Power Motor Driver 36v20 CS with its specification in Table 8 which outputs the commanded voltages to the coils while feeding back the current sensing after receiving the Pulse Width Modulation(PWM) from the SpeedGoat (10). For the detailed wiring diagrams Figures (15,16, 17, 18, 19,and 20).

Table 5. RSP 2000-24: 2000W Single Output Power Supply Specification

Specification		
Output	DC Voltage	24V
	Rated Current	80A
	Current Range	0 80A
	Rated Power	1920W
	Voltage ADJ. Range	21 28V
Input	Voltage Range	90 264VAC 127 370VDC
	Frequesncy Ranget	47 63Hz
	Efficiency	90.5%
	AC Current	16A/115VAC 10A/230VAC
	Leakage Current	<2mA/240VAC

Table 6. RSP 750-24: 750W Single Output Power Supply Specification

Specification		
Output	DC Voltage	24V
	Rated Current	31.3A
	Current Range	0 31.3A
	Rated Power	751.2W
	Voltage ADJ. Range	20 26.4V
Input	Voltage Range	90 264VAC 127 370VDC
	Frequesncy Ranget	47 63Hz
	Efficiency	90.5%
	AC Current	8.2A/115VAC 3.9A/230VAC
	Leakage Current	<2mA/240VAC

Table 7. RS 15-24: 15W Single Output Switching Power Supply Specification

Specification		
Output	DC Voltage	24V
	Rated Current	0.625A
	Current Range	0 0.625A
	Rated Power	15W
	Voltage ADJ. Range	22 27.6V
Input	Voltage Range	85 264VAC 120 370VDC
	Frequesncy Ranget	47 63Hz
	Efficiency	82%
	AC Current	0.35A/115VAC 0.25A/230VAC
	Leakage Current	<2mA/240VAC

Table 8. Pololu High-Power Motor Driver 36v20 CS Specification

General specifications	
Motor channels:	1
Size:	1.8" x 1.2"
Weight:	7 g
Minimum operating voltage:	5.5 V
Maximum operating voltage:	50 V
Continuous output current per channel:	20 A2
Current sense:	0.066 V/A3
Maximum PWM frequency:	40 kHz
Maximum logic voltage:	5.5 V
MOSFET on-resistance (max per leg):	4.8 $m\Omega$
Reverse voltage protection:	N

Table 9. Pinout: Pololu High-Power Motor Driver 36v20 CS

PIN	Default State	Description
V+		This is the main 5.5 - 50 V (absolute max) motor power supply connection, which should typically be made to the larger V+ pad. The smaller V+ pads along the long side of the board are intended for power supply capacitors, and the smaller V+ pad on the logic side of the board gives you access to monitor the motor's power supply (it should not be used for high current).
5V (out)		This regulated 5V output provides a few milliamps. It can be shorted to VCS to power the current sensor. This output should not be connected to other external power supply lines. Be careful not to accidentally short this pin to the neighboring V+ pin while power is being supplied as doing so will instantly destroy the board!
VCS		Connect 5 V to this pin to power the current sensor.
GND		Ground connection for logic and motor power supplies.
CS		ACS714 current sensor output (66 mV/A centered at 2.5 V).
OUTA		A motor output pin.
OUTB		B motor output pin.
PWMH	LOW	Pulse width modulation input: a PWM signal on this pin corresponds to a PWM output on the motor outputs.
PWML	HIGH	Control input that enables coasting when both PWML and PWMH are low.
DIR	LOW	Direction input: when DIR is high current will flow from OUTA to OUTB, when it is low current will flow from OUTB to OUTA.
RESET	HIGH	The RESET pin is pulled up to V+ through a 20 $k\Omega$ resistor. When held low, it puts the driver into a low-power sleep mode and clears any latched fault flags.
FF1	LOW	Fault flag 1 indicator: FF1 goes high when certain faults have occurred.
FF2	LOW	Fault flag 2 indicator: FF2 goes high when certain faults have occurred.

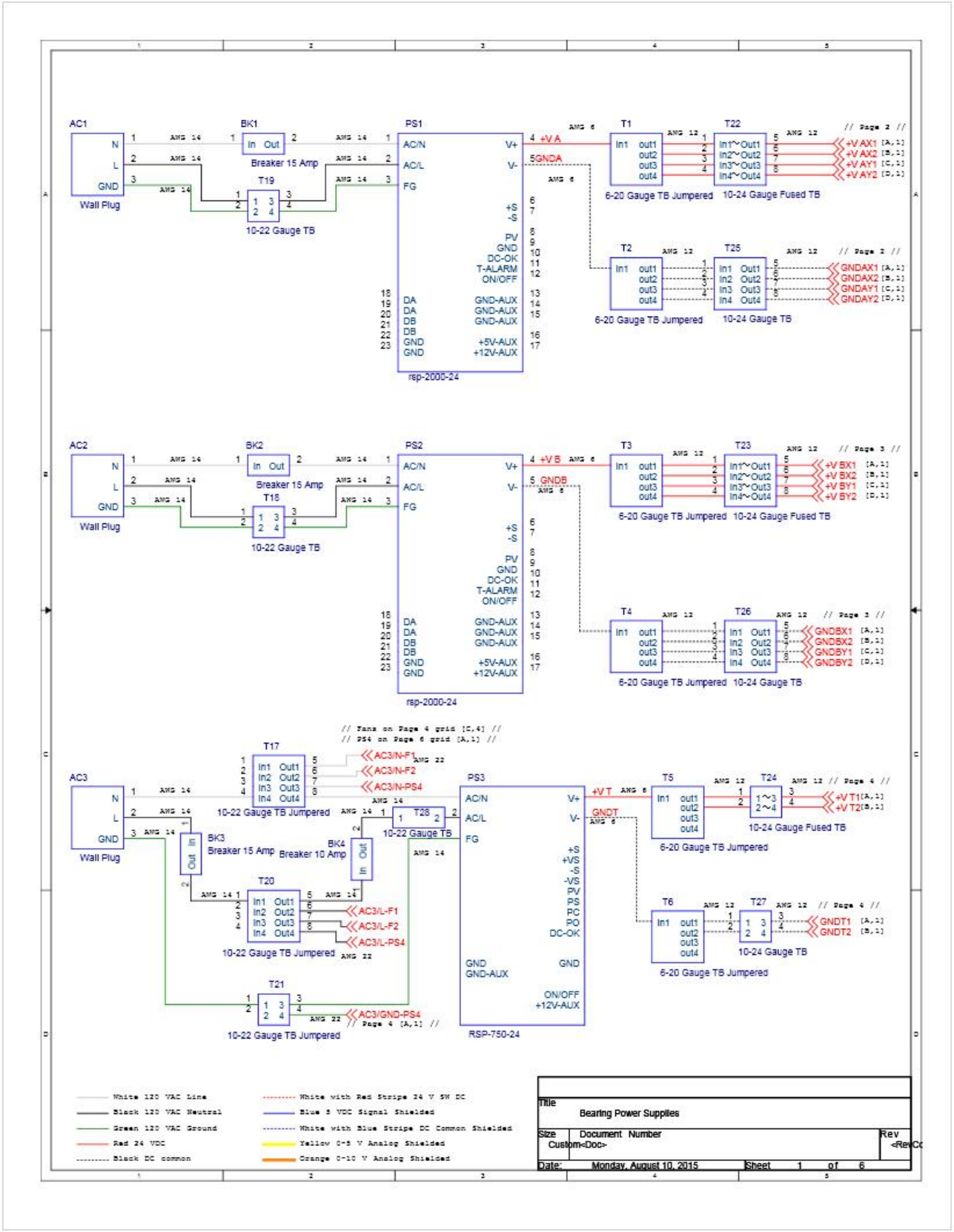

Fig. 15. Bearing Power Supplies

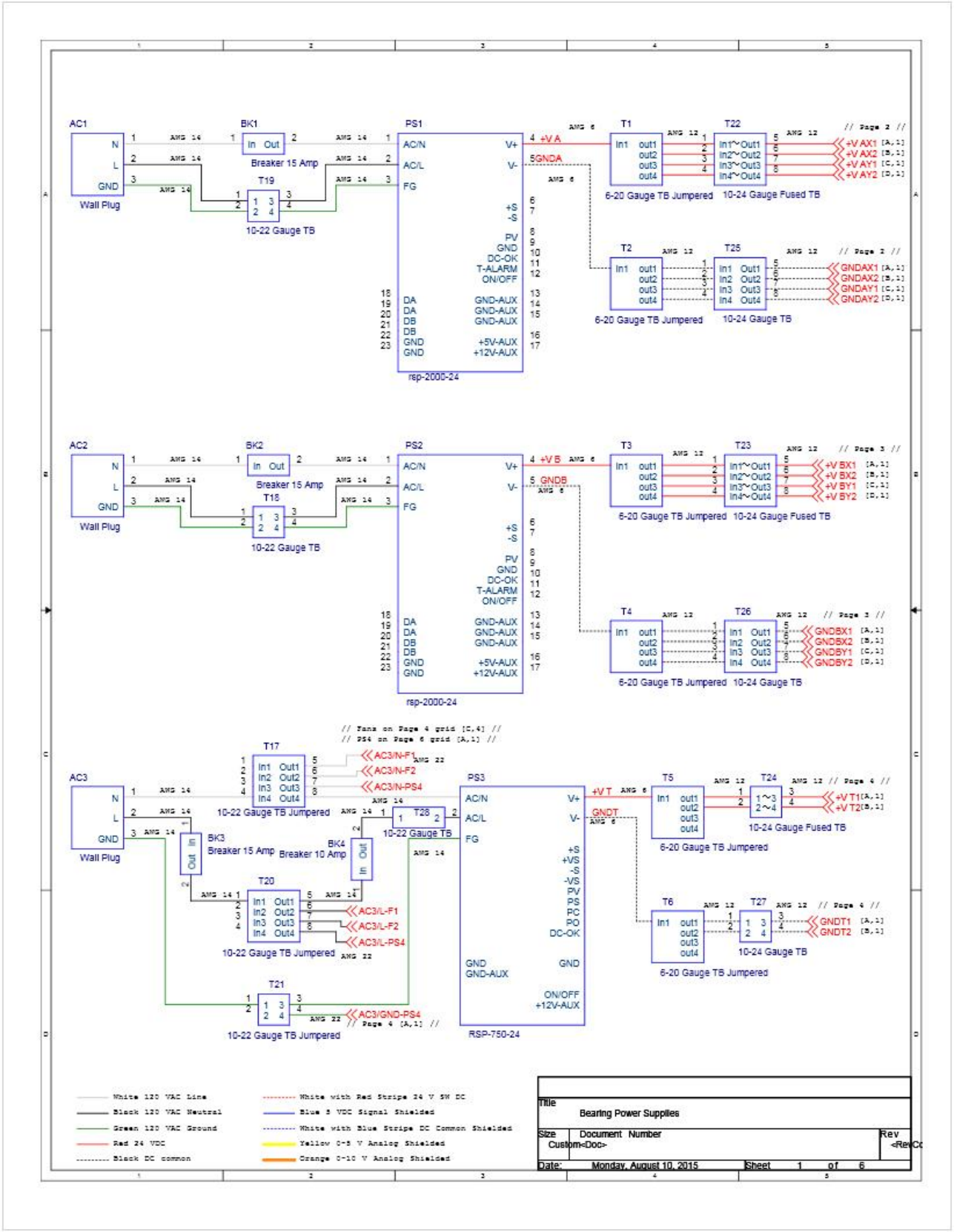

Fig. 16. Bearing A Drives

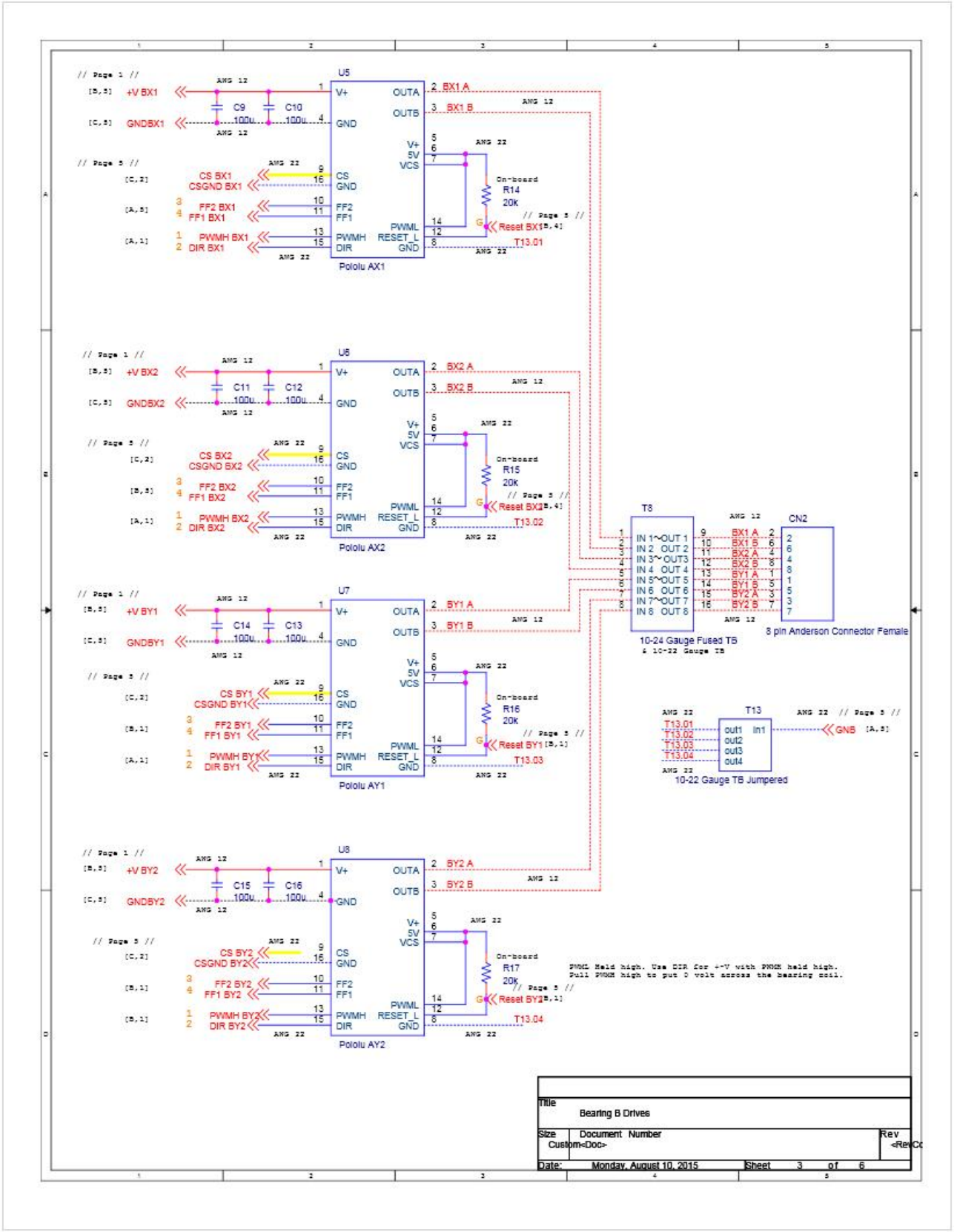

Fig. 17. Bearing B Drives

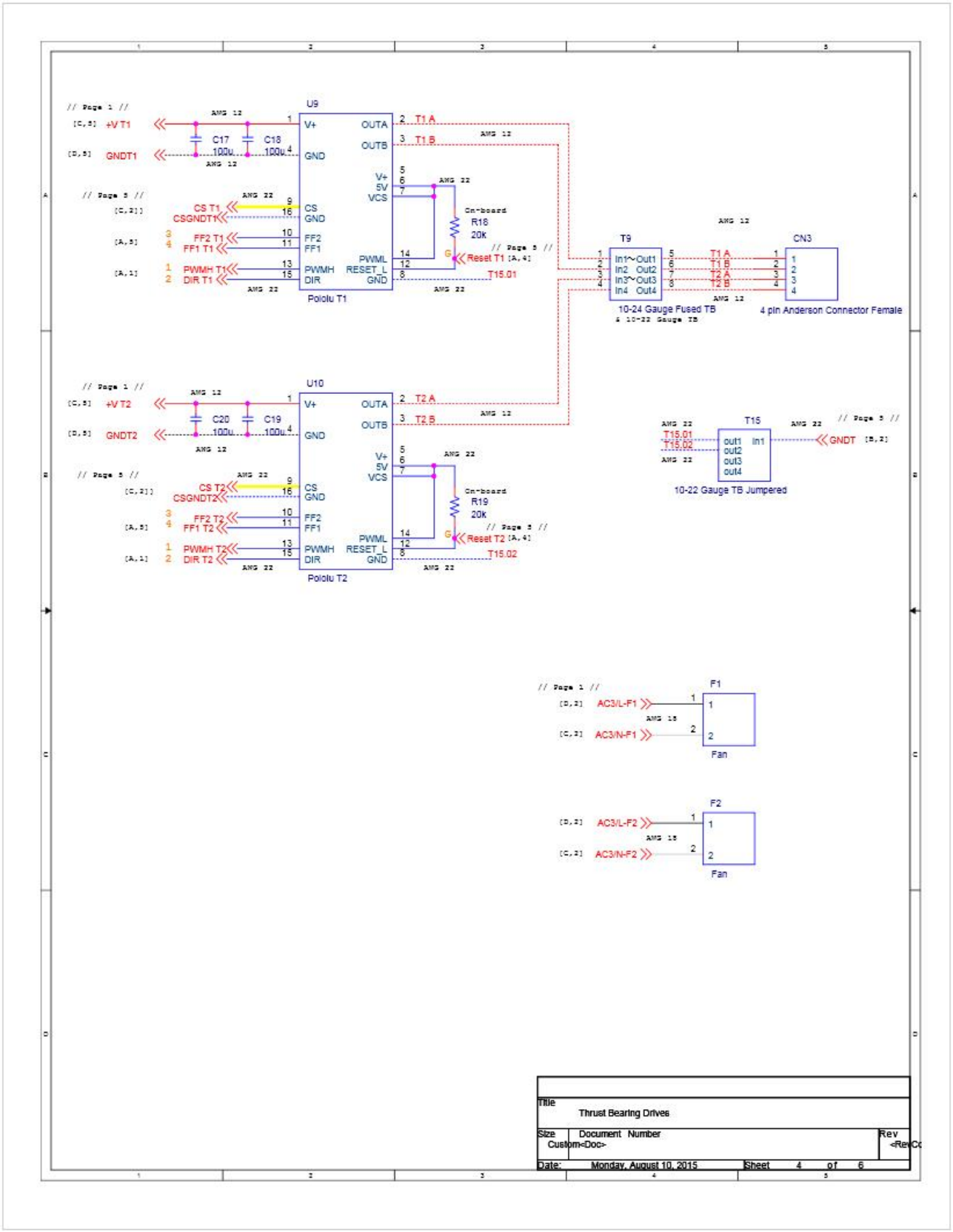

Fig. 18. Thrust Bearing Drives

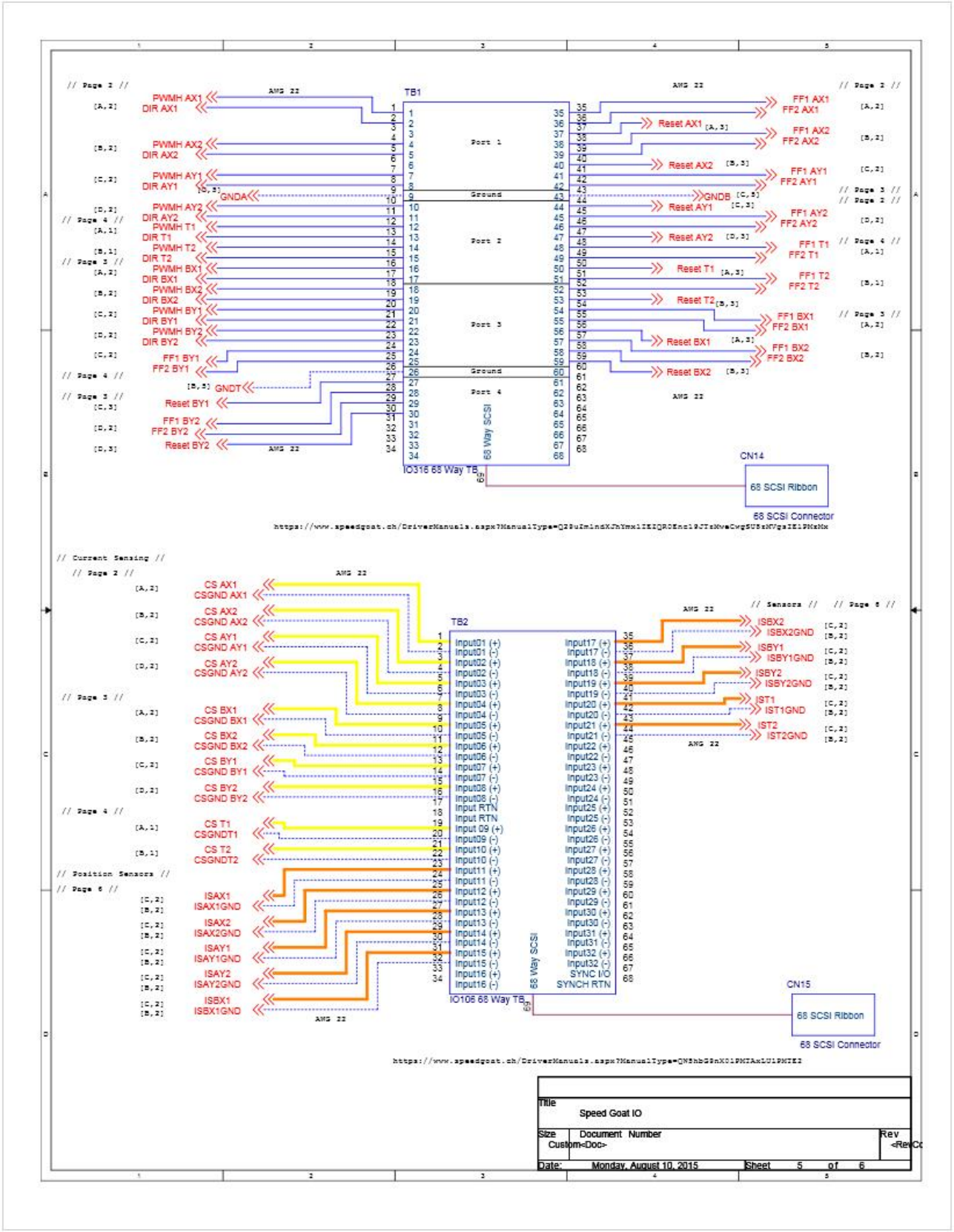

Fig. 19. Speedgoat I/O

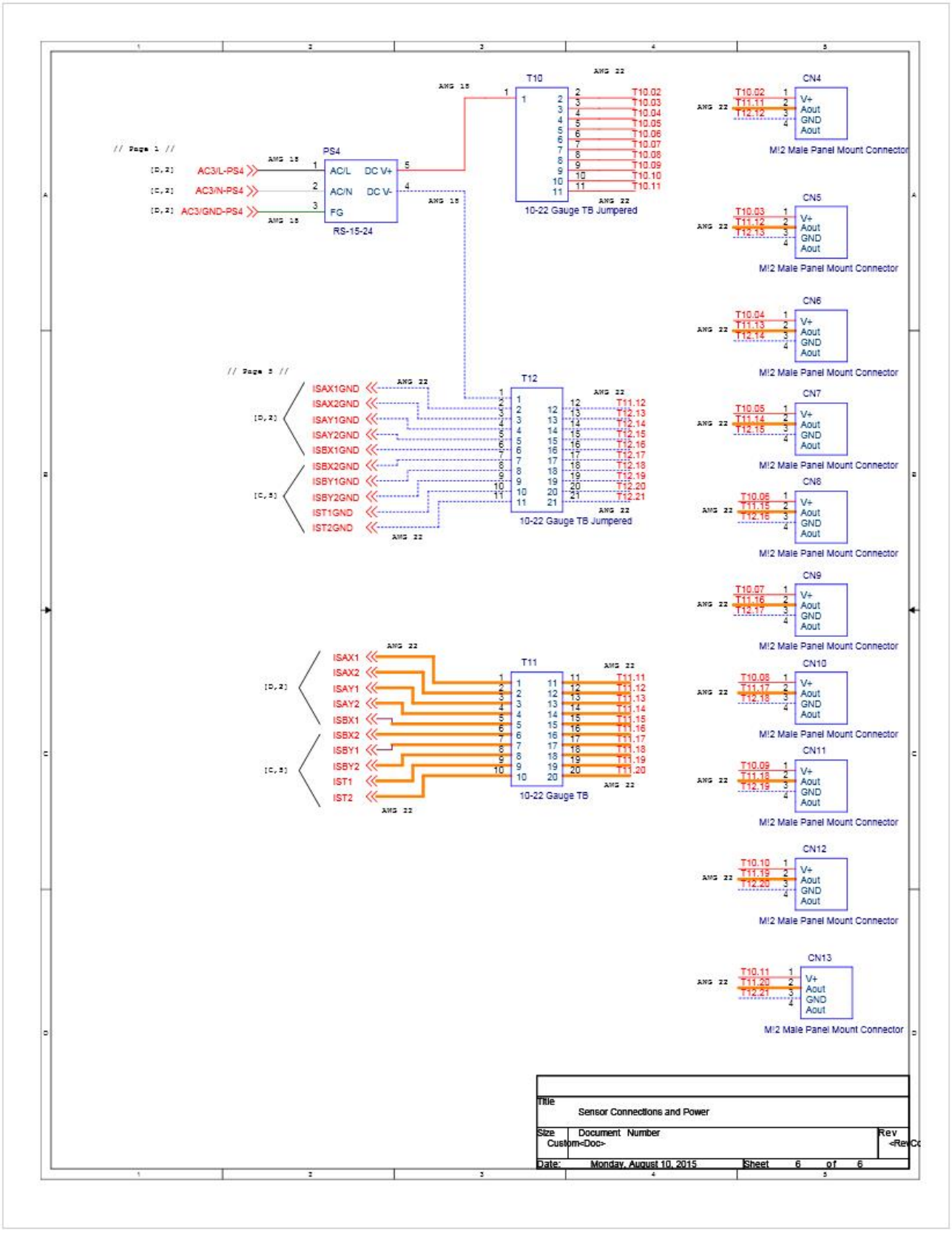

Fig. 20. Sensor Connections and Power

4.3 Control Hardware

In this section, the control hardware used to accomplish the bench-scale testbed design is the Speedgoat performance real-time target machine shown in Figure 21, its specification is shown in Table 10, and its I/O pin mapping is shown in Figures 23 and 22.

Fig. 21. Speedgoat: Performance Real-Time Target Machine

Table 10. Speedgoat: Performance Real-Time Target Machine Specification

Main Board	CPU
Processor	Intel Core i7-3770K 3.5 GHz
Chipset	Intel C216 Express
Bus	PCI, 32-bit/33MHz
Graphics	Intel HD Graphics 400P onboard
USB	4 x USB 3.0 and 1 x USB 2.0 at front
	6 x USB 2.0 internal
Ethernet	2 x Gigabit at front
Serial Ports	1 x RS232/422/485 at front
(for baud rates up to 115kb/s only)	1 x RS232/422/485 and 4 x RS232 internal
Memory	4096MB
BIOS	American Megatrend Inc. (AMI) BIOS
Drives	
Main drive (C:)	250GB Solid State Drive
Power	
Power inlet	AC 100-240V, 50/60Hz, at rear
Power switch	at rear
Secondary power switch	at front
Reset button	none (secondary power switch)
Power LED	at front (combined with secondary power switch)
Environment	
Temperature	0° to $+60^\circ C$ (operating)
Humidity	10-90%, non-condensing
Software	
OS / RTOS	FreeDOS / Simulink Real-Time kernel, preinstalled on CompactFlash
	or Hard Disk for current release of MathWorks software
Development computer	Utilities for kernel transfer,
	I/O drivers and Simulink test models for your selected I/O modules

Pin on Term. Board	Code Module Channel (Vector)	Inp.: 0 Outp.: 1	Functionality	Trans ceiver
1	1	1	PWM - A	TTL
2			PWM - B	TTL
3			PWM - Trigger	TTL
4	2	1	PWM - A	TTL
5			PWM - B	TTL
6			PWM - Trigger	TTL
7	3	1	PWM - A	TTL
8			PWM - B	TTL
9			Ground	
10	4	1	PWM - A	TTL
11			PWM - B	TTL
12	5	1	PWM - A	TTL
13			PWM - B	TTL
14	6	1	PWM - A	TTL
15			PWM - B	TTL
16	7	1	PWM - A	TTL
17			PWM - B	TTL
18	8	1	PWM - A	TTL
19			PWM - B	TTL
20	9	1	PWM - A	TTL
21			PWM - B	TTL
22	10	1	PWM - A	TTL
23			PWM - B	TTL
24	1	0/1	DIO	TTL
25	2	0/1	DIO	TTL
26			Ground	
27	3	0/1	DIO	TTL
28	4	0/1	DIO	TTL
29	5	0/1	DIO	TTL
30	6	0/1	DIO	TTL
31	7	0/1	DIO	TTL
32	8	0/1	DIO	TTL
33	9	0/1	DIO	TTL
34	10	0/1	DIO	TTL

Pin on Term. Board	Code Module Channel (Vector)	Inp.: 0 Outp.: 1	Functionality	Trans ceiver	Port	Pull-Resistors
35	11	0/1	DIO	TTL	1	pull-up 3.3 VDC, weak pull-up 5.0 VDC, pull-down, floating
36	12	0/1	DIO	TTL		
37	13	0/1	DIO	TTL		
38	14	0/1	DIO	TTL		
39	15	0/1	DIO	TTL		
40	16	0/1	DIO	TTL		
41	17	0/1	DIO	TTL		
42	18	0/1	DIO	TTL		
43			Ground			
44	19	0/1	DIO	TTL	2	pull-up 3.3 VDC, weak pull-up 5.0 VDC, pull-down, floating
45	20	0/1	DIO	TTL		
46	21	0/1	DIO	TTL		
47	22	0/1	DIO	TTL		
48	23	0/1	DIO	TTL		
49	24	0/1	DIO	TTL		
50	25	0/1	DIO	TTL		
51	26	0/1	DIO	TTL		
52	27	0/1	DIO	TTL	3	pull-up 3.3 VDC, weak pull-up 5.0 VDC, pull-down, floating
53	28	0/1	DIO	TTL		
54	29	0/1	DIO	TTL		
55	30	0/1	DIO	TTL		
56	31	0/1	DIO	TTL		
57	32	0/1	DIO	TTL		
58	33	0/1	DIO	TTL		
59	34	0/1	DIO	TTL		
60			Ground			
61	35	0/1	DIO	TTL	4	pull-up 3.3 VDC, weak pull-up 5.0 VDC, pull-down, floating
62	36	0/1	DIO	TTL		
63	37	0/1	DIO	TTL		
64	38	0/1	DIO	TTL		
65	39	0/1	DIO	TTL		
66	1	0	Interrupt Input	TTL		
67	1	0	Negation Input	TTL		
68		1	Negation Output	TTL		

Fig. 22. I/O Pin Mapping for IO316 FPGA

Pin	Signal *Single ended mode*	Signal *Pseudo Differential mode*	Signal *Differential mode*	Pin	Signal *Single ended mode*	Signal *Pseudo Differential mode*	Signal *Differential mode*
1	Input01	Input (-) ('remote sense')	Input01 (+)	35	Input33	Input32	Input17 (+)
2	Input02	Input01	Input01 (-)	36	Input34	Input33	Input17 (-)
3	Input03	Input02	Input02 (+)	37	Input35	Input34	Input18 (+)
4	Input04	Input03	Input02 (-)	38	Input36	Input35	Input18 (-)
5	Input05	Input04	Input03 (+)	39	Input37	Input36	Input19 (+)
6	Input06	Input05	Input03 (-)	40	Input38	Input37	Input19 (-)
7	Input07	Input06	Input04 (+)	41	Input39	Input38	Input20 (+)
8	Input08	Input07	Input04 (-)	42	Input40	Input39	Input20 (-)
9	Input09	Input08	Input05 (+)	43	Input41	Input40	Input21 (+)
10	Input10	Input09	Input05 (-)	44	Input42	Input41	Input21 (-)
11	Input11	Input10	Input06 (+)	45	Input43	Input42	Input22 (+)
12	Input12	Input11	Input06 (-)	46	Input44	Input43	Input22 (-)
13	Input13	Input12	Input07 (+)	47	Input45	Input44	Input23 (+)
14	Input14	Input13	Input07 (-)	48	Input46	Input45	Input23 (-)
15	Input15	Input14	Input08 (+)	49	Input47	Input46	Input24 (+)
16	Input16	Input 15	Input08(-)	50	Input48	Input47	Input24 (-)
17	Input RTN	Input RTN	Input RTN	51	Input49	Input48	Input25 (+)
18	Input RTN	Input RTN	Input RTN	52	Input50	Input49	Input25 (-)
19	Input17	Input16	Input09 (+)	53	Input51	Input50	Input26 (+)
20	Input18	Input17	Input09 (-)	54	Input52	Input51	Input26 (-)
21	Input19	Input18	Input10 (+)	55	Input53	Input52	Input27 (+)
22	Input20	Input19	Input10 (-)	56	Input54	Input53	Input27 (-)
23	Input21	Input20	Input11 (+)	57	Input55	Input54	Input28 (+)
24	Input22	Input21	Input11 (-)	58	Input56	Input55	Input28 (-)
25	Input23	Input22	Input12 (+)	59	Input57	Input56	Input29 (+)
26	Input24	Input23	Input12 (-)	60	Input58	Input57	Input29 (-)
27	Input25	Input24	Input13 (+)	61	Input59	Input58	Input30 (+)
28	Input26	Input25	Input13 (-)	62	Input60	Input59	Input30 (-)
29	Input27	Input26	Input14 (+)	63	Input61	Input60	Input31 (+)
30	Input28	Input27	Input14 (-)	64	Input62	Input61	Input31 (-)
31	Input29	Input28	Input15 (+)	65	Input63	Input62	Input32 (+)
32	Input30	Input29	Input15 (-)	66	Input64	Input63	Input32 (-)
33	Input31	Input30	Input16 (+)	67	SYNC I/O	SYNC I/O	SYNC I/O
34	Input32	Input31	Input16 (-)	68	SYNCH RTN	SYNCH RTN	SYNCH RTN

Fig. 23. I/O Pin Mapping for IO106

4.4 Control Algorithm

In this section, models of the AMBs will be used to develop and characterize different control system formulations. The primary single-variable control design technique used for a large number of linear systems is the proportional integral derivative (PID) controller. The next control design technique that will be applied is the linear quadratic regulator (LQR) controller. This technique can improve the system response by taking advantage of the coupling between the orthogonal axes due to gyroscopic effects and fluid rotor interactions. While some simulation results are shown in this section, its primary purpose is to describe the mathematical development of the control system.

The basic system expressed in the COM coordinates system is given by Eg. (33). The rotor position is given by Euclidean coordinates of the COM $z = [x, y, \theta_x, \theta_y]^T$, where x and y are the radial translations and θ_x and θ_y are the rotations around the x and y axes, respectively. The equation of motion is given by

$$M\ddot{z} + (G + C_b B^T)\dot{z} + K_b B^T z = u(t), \tag{33}$$

where M is the symmetric mass/inertia matrix, G is the skew-symmetric gyroscopic matrix, $C_b = C_b^T \geq 0$ is the damping matrix, K is the symmetric stiffness matrix, $K_b = -K_b^T$ is the *nonconservative* stiffness matrix, B^T is a transformation from the AMB coordinate system to the COM coordinate system, and $u(t)$ are the external forces.

4.4.1 Final System Model

In designing the control system gains, it is desirable to express the AMBs as a linear state-space system. There are two basic coordinate systems that have physical meaning – the coordinates that describe the movement of the COM of the rotor and the coordinates that describe the actuation of the bearings in the bearing coordinate system. This requires a state change from the COM coordinate system $z = [x, y, \theta_x, \theta_y]^T$ to the bearing coordinate system $z_b = [x_A, y_A, x_B, y_B]^T$, where A denotes the axial bearing that is L_A m away from the COM opposite the impeller and B denotes the axial bearing that is L_B m from the COM closest to the impeller. The coordinate linearized transformation is given by

$$z_b = B^T z = \begin{bmatrix} 1 & 0 & -L_A & 0 \\ 0 & 1 & 0 & -L_A \\ 1 & 0 & L_B & 0 \\ 0 & 1 & 0 & L_B \end{bmatrix}. \tag{34}$$

The input states $u(t)$ are chosen to be the bearing forces $u_b = [f_{xA}, f_{yA}, f_{xB}, f_{yB}]^T$. Translating the inputs from the bearing coordinate system $u_b(t)$ to the COM coordinate system $u(t)$, the input is given by

$$u = Bu_b = \begin{bmatrix} 1 & 0 & 1 & 0 \\ 0 & 1 & 0 & 1 \\ -L_A & 0 & L_B & 0 \\ 0 & -L_A & 0 & L_B \end{bmatrix}, \tag{35}$$

which is identical to the transpose of B^T. The linearized bearing derived in Sect. 4.2.1 acting in the AMB coordinate system can be expressed using the rotor COM states $z(t)$ and the coil currents $i(t)$ by

$$u_b(t) = -K_s B^T z(t) + K_i i(t), \tag{36}$$

where $K_s = diag(k_s, k_s, k_s, k_s)$, $K_i = diag(k_i, k_i, k_i, k_i)$, and k_s and k_i are given in Table 3. The bearing forces u_b in the AMB coordinate system can in turn be translated to the COM coordinate system using

$$u(t) = -BK_sB^T z(t) + BK_i i(t). \tag{37}$$

Finally, after the appropriate transformations are applied, the second-order linearized ordinary differential equation (ODE) in COM coordinates is given by

$$M\ddot{z}(t) + (G + C_bB^T)\dot{z}(t) + (K_bB^T + BK_sB^T)z(t) = BK_i i(t). \tag{38}$$

Transforming Eq. (38) into a state-space formulations yields

$$\begin{aligned} \dot{x}(t) &= \mathbf{A}x(t) + \mathbf{B}u(t) = \begin{bmatrix} \mathbf{0}^{4\times4} & \mathbf{I}^{4\times4} \\ -M^{-1}(K_bB^T + BK_sB^T) & -M^{-1}(G + C_bB^T) \end{bmatrix} x(t) + \begin{bmatrix} \mathbf{0}^{4\times4} \\ M^{-1}BK_i \end{bmatrix} u(t) \text{ and} \\ y(t) &= \mathbf{C}x(t) = \begin{bmatrix} B^T & \mathbf{0}^{4\times4} \end{bmatrix} x(t), \end{aligned} \tag{39}$$

where $x(t) = [x, y, \theta_x, \theta_y, \dot{x}, \dot{y}, \dot{\theta}_x, \dot{\theta}_y]^T$ is the system state, $y(t)$ is the vector of position sensor measurements in the bearing coordinate system, and $\mathbf{I}^{4\times4}$ is an identity matrix. In this case, $y(t) \equiv z_b(t)$ and the control variable $u(t)$ in this formulation is the bearing coil current vector $i(t)$. Substituting the actual values in Eq. 39 gives the following:

$$\begin{aligned} A &= \begin{bmatrix} 0 & 0 & 0 & 0 & 1 & 0 & 0 & 0 \\ 0 & 0 & 0 & 0 & 0 & 1 & 0 & 0 \\ 0 & 0 & 0 & 0 & 0 & 0 & 1 & 0 \\ 0 & 0 & 0 & 0 & 0 & 0 & 0 & 1 \\ 2105 & 0 & 18.6 & 0 & -0.2 & 0 & 0 & 0 \\ 0 & 2105 & 0 & 18.6 & 0 & -0.2 & 0 & 0 \\ 899.3 & 0 & 1838.1 & 0 & -9.8 & 2.3 & -1.4 & 0.3 \\ 0 & 899.3 & 0 & 1838.1 & 2.3 & -9.8 & -0.2 & -1.4 \end{bmatrix} \\ B &= \begin{bmatrix} 0 & 0 & 0 & 0 \\ 0 & 0 & 0 & 0 \\ 0 & 0 & 0 & 0 \\ 0 & 0 & 0 & 0 \\ 0.5541 & 0 & 0.5541 & 0 \\ 0 & 0.5541 & 0 & 0.5541 \\ 3.8750 & 0 & -3.3873 & 0 \\ 0 & 3.8750 & 0 & -3.3873 \end{bmatrix} \\ C &= \begin{bmatrix} 1 & 0 & 0.1413 & 0 & 0 & 0 & 0 & 0 \\ 0 & 1 & 0 & 0.1413 & 0 & 0 & 0 & 0 \\ 1 & 0 & -0.1235 & 0 & 0 & 0 & 0 & 0 \\ 0 & 1 & 0 & -0.1235 & 0 & 0 & 0 & 0 \end{bmatrix} \\ D &= \mathbf{0} \end{aligned} \tag{40}$$

4.4.2 Inner Current Control Loop

To simplify the operation of the controller, the coil currents are controlled independently by an inner current control loop, while the rotor position is controlled by a separate controller. The block diagram for the inner current control loop is shown in Figure 24 The current control loop is designed so improve the

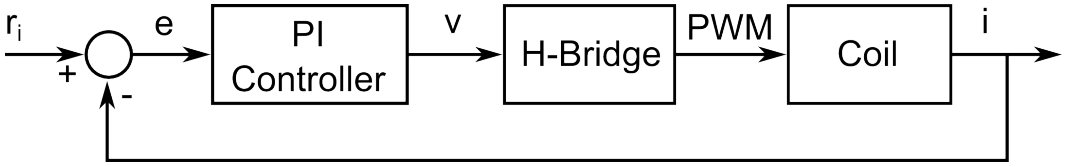

Fig. 24. Inner current control loop for a single coil

bandwidth of the H-Bridge current drivers and more accurately control the current commands. This loop utilizes the built in current sensors from the H-Bridge drivers. The coil dynamics are given by a resistor and inductor in series.

$$L\frac{di(t)}{dt} + Ri(t) = v(t) \tag{41}$$

The controller used to improve the performance of the H-Bridge drivers is

$$v(t) = -K_P e(t) - \int_t K_I e(t) \tag{42}$$

where $e(t) = r_i(t) - i(t)$ is the difference between the commanded current and the measured current.

In Figure 25, the step response of the current feedback loop is shown. The reference command is one amp for one second. The controller gains are $K_P = 1.2$ and $K_I = 300$. The graph shows a nonzero voltage command from 0-1 seconds and 2-4 seconds. This is due to a deadband on the H-Bridges at low voltage commands. In Figure 26, the rise times of the open loop response of the H-Bridge and the closed-loop response with the feedback controller are shown. The feedback controller has a 10 ms rise time which is three times faster than the open-loop response. The measured coil resistance and inductance for the coil tested in this section are $R = 0.217\ \Omega$ and $L = 785.5\ \mu H$ respectively. The values for all other coils when measured were similar. These values were measured statically from the plug to the coil so there are uncertainties in the actual values for the coil inductance and resistance for the complete system. To more accurately identify the coil parameters, the open loop response was used to identify the coil transfer function as

$$I(s) = \frac{884.9}{s + 217.9}V(s) \tag{43}$$

The comparison between the identified coil equation and the measure response is shown in Figure 27. This gives an effective resistance for the coil of $R = 0.2462\ \Omega$ and an effective inductance of $L = 1130\ \mu H$.

4.4.3 Outer Position Control Loop

To begin system identification and model validation of the bearing rotordynamics, an initial decoupled PID controller was developed to stabilize the shaft. This is necessary because system identification techniques require bounded responses which can only be achieved with a stable system. The outer position control loop block diagram is shown in Figure 28.

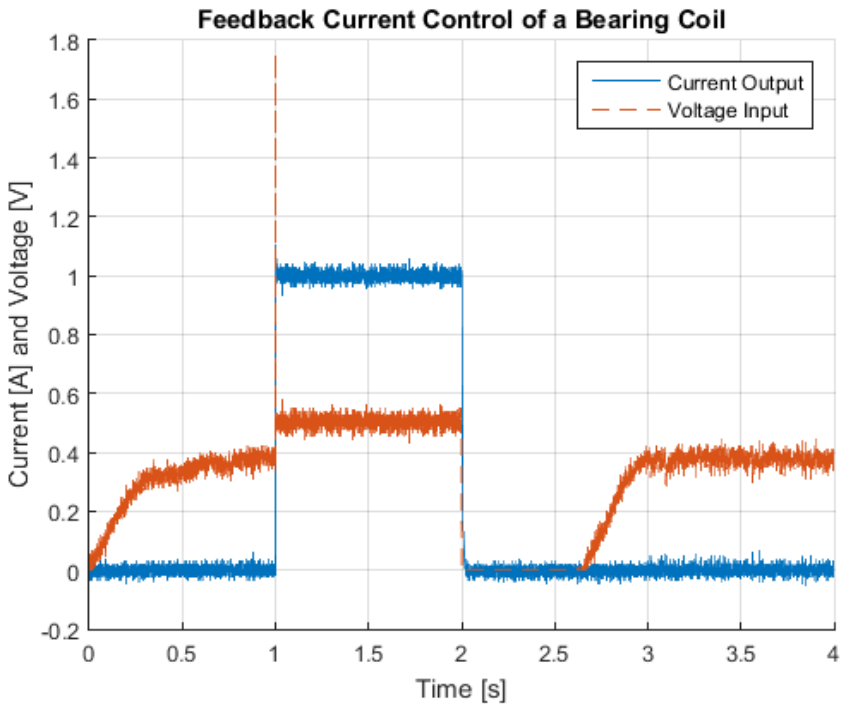

Fig. 25. Step Response of the Inner Current Loop

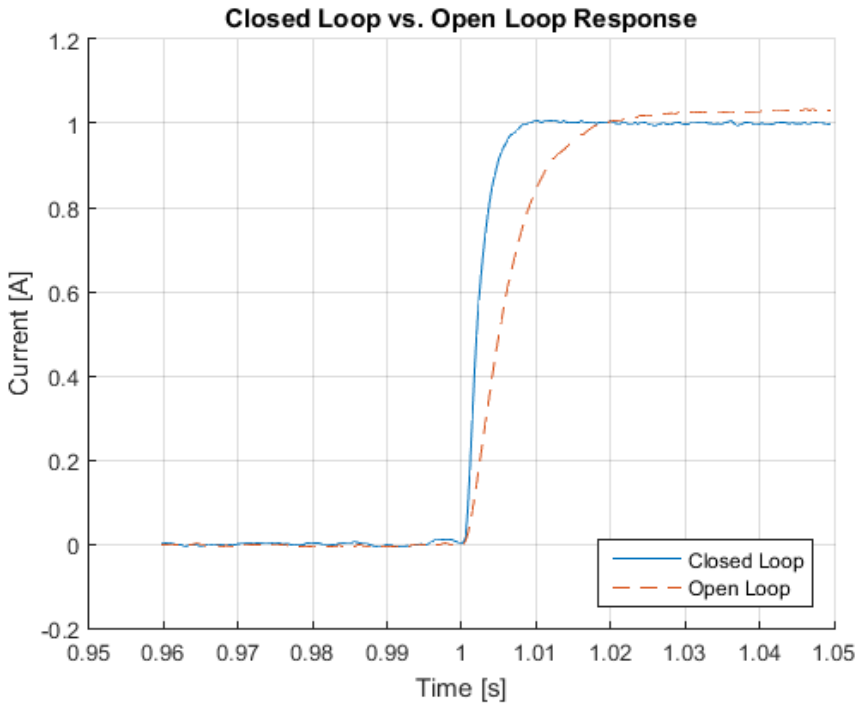

Fig. 26. A comparison of the rise times of the open loop current response vs. the feedback controller response.

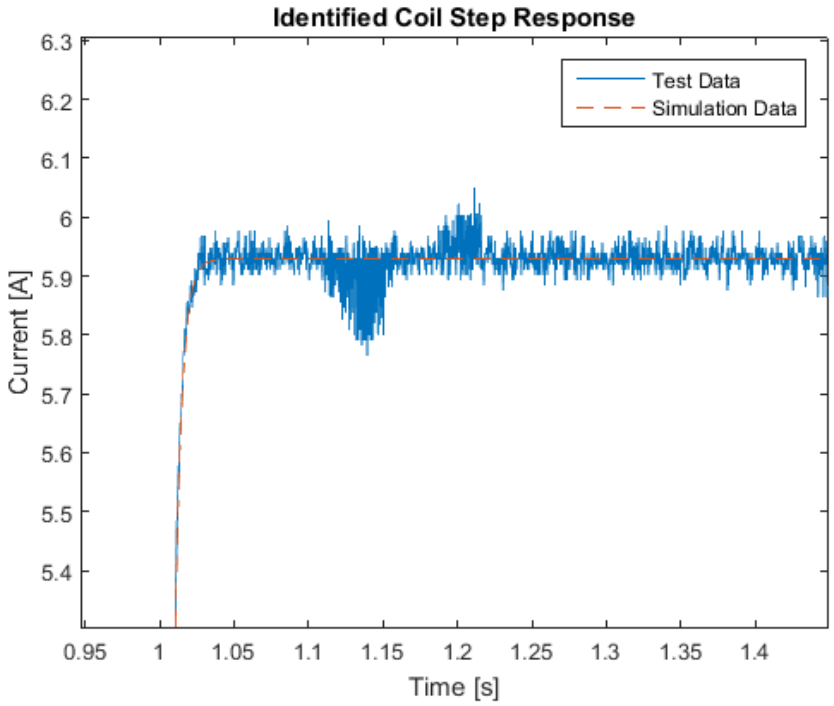

Fig. 27. A comparison between the measured open loop step response of a bearing coil and the identified step response.

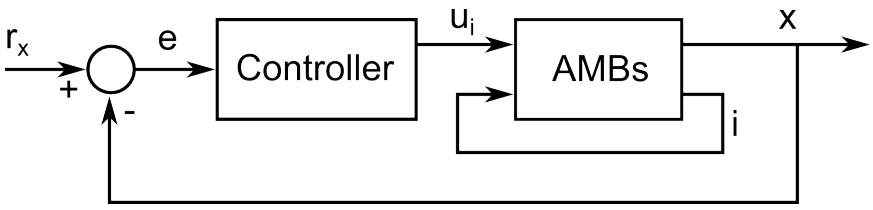

Fig. 28. Outer position control loop for a single coil

Applying a local PID controller to each bearing axis is equivalent to

$$i_{xA} = -k_{Px}x_A - k_{Ix}\int_t e_{xA} - k_{Dx}\dot{x}_A, \tag{44}$$

$$i_{yA} = -k_{Py}y_A - k_{Iy}\int_t e_{yA} - k_{Dy}\dot{y}_A, \tag{45}$$

$$i_{xB} = -k_{Px}x_B - k_{Ix}\int_t e_{xB} - k_{Dx}\dot{x}_B, \text{ and} \tag{46}$$

$$i_{yB} = -k_{Py}y_B - k_{Iy}\int_t e_{yB} - k_{Dy}\dot{y}_B. \tag{47}$$

where e_{xA}, e_{yA}, e_{xB}, and e_{yB} are the errors between the reference inputs and the current system states. In state-space notation, this becomes

$$u(t) = -(K_P y + K_I \int y + K_D \dot{y}), \tag{48}$$

where $K_P = diag(k_{PA}, k_{PA,}k_{PB}, k_{PB})$, $K_I = diag(k_{IA}, k_{IA}, k_{IB}, k_{IB})$, and $K_D = diag(k_{DA}, k_{DA}, k_{DB}, k_{DB})$. Replacing the PID values from our simulation which stabilized the our AMB gives the following: $K_P = diag(-2900, -4500, -2900, -4500)$, $K_I = diag(-370, -381, -370, -381)$, and $K_D = diag(-1950, -14500, -1950, -14500)$. This assumes that the sensors are collocated with the AMBs. Substituting Eg. (48) into the closed-loop equation of motion is

$$M\ddot{z} + (G + C_b B^T)\dot{z} + (K_b B^T + BK_s C)z = -BK_i K_P B^T z - BK_i K_I \int (r(t) - B^T z) - BK_i K_D \dot{z}. \tag{49}$$

Representing Eg. (49) in state-space form requires an augmentation of the system states $x(t)$ by the state $x_i(t) = e(t) = r(t) - B^T z(t)$.[6] The augmented closed-loop differential equation becomes

$$\begin{aligned} \begin{bmatrix} \dot{x} \\ \dot{x}_i \end{bmatrix} &= \begin{bmatrix} \mathbf{A} & \mathbf{B}K_I \\ -B^T & \mathbf{0}^{4\times 8} \end{bmatrix} \begin{bmatrix} x \\ x_i \end{bmatrix} + \begin{bmatrix} \mathbf{0}^{8\times 4} \\ \mathbf{I}^{4\times 4} \end{bmatrix} r(t) \text{ and} \\ y &= \begin{bmatrix} \mathbf{C} & \mathbf{0}^{4\times 4} \end{bmatrix} \begin{bmatrix} x \\ x_i \end{bmatrix}, \end{aligned} \tag{50}$$

where $\mathbf{A}$, $\mathbf{B}$, and $\mathbf{C}$ are from Eg. (39) [7]. The additional states add four additional eigenvalues and modify the existing eigenvalues of $\mathbf{A}$ [1].

Figure 29 shows the step response of the position controller to a 0.0001 mm step command. The current stabilizing controller shows considerable overshoot during the response. This is due to the controller designed to stabilize the system from an initial position with an airgap of 0.0035 mm. This large initial airgap and large variation of the system parameters as the shaft moves means that the controller gains need to be conservative for stable operation. The conservative controller gains lead to the large overshoot and slow integral response of the controller. However, this is sufficient for system identification.

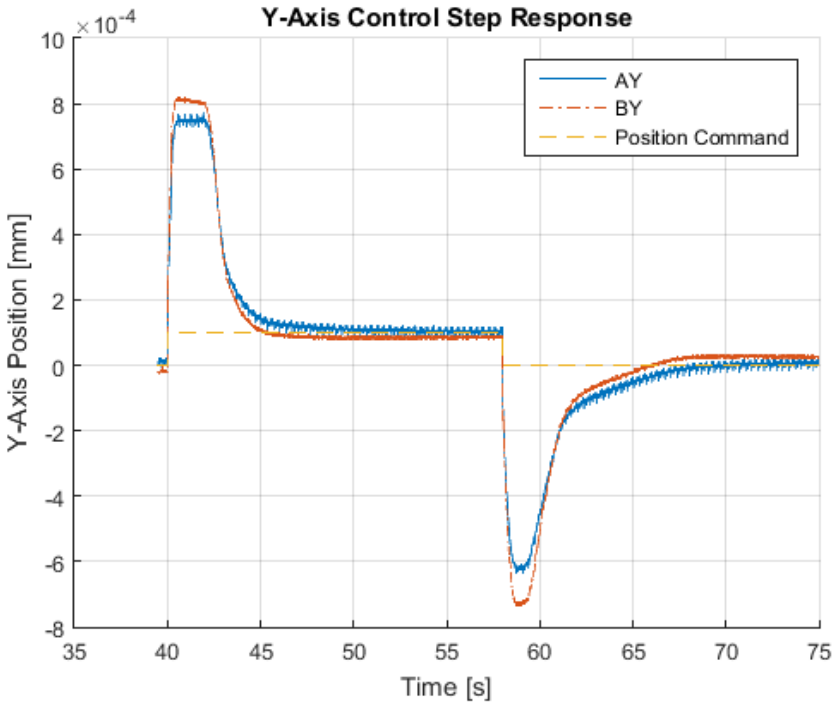

Fig. 29. Y-Axis Control Step Response

5 CONCLUSIONS AND FUTURE WORK

This report details the mechanical, electromagnetic, and initial stabilizing controller design for an embedded I&C testbed that features active magnetic bearings. The mechanical design was focused on flexibility and low weight to create the option for testing the response of control systems to variations in physical parameters while being portable. The electromagnetic design was optimized to maximize the force to mass ratio of the magnetic bearings while meeting the *a priori* geometric constraints and force requirements. The initial coil windings had a significantly lower packing factor than expected and new coils will be wound in the future to achieve a packing factor closer to face centered cubic. The power electronics were designed to be flexible and specified to meet the current requirements developed during the electromagnetic design. After testbed assembly, the Speedgoat rapid control development platform was set up and the inputs and outputs configured. An inner current control loop was designed and tested to simplify the design of the position controller and increase the bandwidth of the current response. Finally, an initial stabilizing position controller was created a a prelude to system identification tasks that will begin in the next phase of testing and design. Future work will involve system identification of the bearing parameters and model validation. This will be followed by developing embedded controllers using advanced control design techniques such as Linear Quadratic methods, robust control, and nonlinear control. The performance of the different controllers will be compared quantitatively. Finally, sensorless bearing control techniques that utilize the physics of the coils in the AMBs will be investigated as a prelude to designing a laboratory scale testbed for *in situ* testing using a hydraulic test loop.

6 REFERENCES

[1] Dennis S. Bernstein. *Matrix Mathematics*. Princeton University Press, 2 edition, 2009.

[2] Luc Burdet. *Active Magnetic Bearing Design and Characterization for High Temperature Applications*. PhD thesis, École Polytechnique Fédérale De Lausanne, 2006.

[3] Roger A. Kisner, Alexander M. Melin, Timothy A. Burress, David L. Fugate, David E. Holcomb, John B. Wilgen, John M. Miller, Dane F. Wilson, Pamela C. Silva, Lynsie J. Whitlow, and Fred J. Peretz. Embedded sensors and controls to improve component performance and reliability: Conceptual design report. Technical report, Oak Ridge National Laboratory ORNL/TM-2012/433, 2012.

[4] Alexander M. Melin, Roger Kisner, and David L. Fugate. Embedded sensors and controls to improve component performance and reliability: System dynamics modeling and control system design. Technical Report ORNL/TM-2013/415, Oak Ridge National Laboratory, 2013.

[5] Gerald Montague, Mark Jansen, Ben Ebihara, Ralph Jansen, Alan Palazzolo, Randy Tucker, Jason Preuss, Andrew Hunt, Jeff Trudell, and Andrew Provenza. Design and fabrication of a high-temperature radial magnetic bearing for turbomachinery. Technical Report NASA/TM-2003-212300, National Aeronautics and Space Administration, 2003.

[6] Norman S. Nise. *Control Systems Engineering*. John Wiley & Sons, 2000.

[7] Raymond T. Stefani, Bahram Shahian, Clement J. Savant Jr., and Gene H. Hostetterq. *Design of Feedback Control Systems*. Oxford University Press, 2002.

[8] Alfons Traxler and Eric Maslen. *Magnetic Bearings: Theory, Design, and Application to Rotating Machinery*. Springer, 2010.